

Transworld Research Network
37/661 (2), Fort P.O., Trivandrum-695 023, Kerala, India



Recent Res. Devel. Biophys., 5(2006): ISBN: 81-7895-215-7

Advances in the mechanical characterization of soft materials by nanoindentation

David C. Lin¹, Emilios K. Dimitriadis², and Ferenc Horkay¹

¹Laboratory of Integrative and Medical Biophysics, ²National Institute of Biomedical Imaging and Bioengineering, National Institutes of Health Bethesda, MD, 20892, U.S.A

Abstract

The emergence of nanoscience has spurred the demand for technologies capable of probing physical phenomena at resolutions down to the atomic length scale. Under this initiative, recent advances in instrumented nanoindentation have made the atomic force microscope and the depth-sensing nanoindenter practical tools in studying the local material properties of a broad array of solid surfaces at microscopic and sub-micron length scales. High resolution capability is especially important in the probing of biological samples, which are typically very inhomogeneous. In this paper, the current state

Correspondence/Reprint request: Dr. David C. Lin, Laboratory of Integrative and Medical Biophysics National Institutes of Health, Bethesda, MD, 20892, U.S.A. E-mail: lindavid@mail.nih.gov

of the field as it pertains to the mechanical characterization of soft solids is reviewed. The spectrum of contact mechanics theories based on linear elasticity and their application to nanoindentation data are presented, followed by a summary of data analysis techniques. The authors' comprehensive algorithm for the automated processing of large collections of data is highlighted and examples are shown to illustrate the robustness of the method. Limitations of the method and other considerations for successful application of nanoindentation to soft materials are discussed.

Introduction

Indentation is a well-established technique in materials testing, with its origins in the field of metallurgy as a means of characterizing hardness [1]. More recently, with the development of miniaturization-enabling technologies (e.g., highly sensitive photodetectors, electrostatic and piezoelectric actuators, sophisticated feedback controls, microfabrication techniques), instrumented nanoindentation has become a widely accepted method for measuring the mechanical properties of thin films and small volumes of material [2, 3]. The two prevalent nanoindentation technologies, both developed in the 1980s and both available commercially, are the depth-sensing nanoindenter (DSN) [4] and the atomic force microscope (AFM) [5], which are shown schematically in Figure 1. Advantages of one system over the other are dependent on its basic design and control scheme. The depth-sensing system, with its basis in electromagnetic or electrostatic force actuation, permits either load-controlled or displacement-controlled indentation and the application of a force perfectly normal to the sample surface. Existing commercial systems, however, lack the hardware for precision scanning applications. In commercial AFMs, fine displacement control in all three axes is typically achieved via piezoelectric actuation. This feature of the AFM contributes to its high-resolution imaging capability. Drawbacks of using the AFM in nanoindentation are chiefly associated with the necessity to match the bending stiffness of the cantilever with the stiffness of the indented sample [2]. For hard surfaces, it may be difficult to achieve adequate penetration depths even with the stiffest cantilevers; conversely in very soft materials, it may be difficult to generate adequate deflection of the cantilever for accurate force measurements. Hybrid systems combining the stable force-modulation inherent in the depth-sensing nanoindenter and the precise scanning hardware of the AFM [6-8] are beginning to attain more widespread adoption by researchers.

Although measurements of hardness and elastic properties remain the predominant implementation of the nanoindentation instruments in mechanical characterization [3, 9, 10], many analytical, physical, and controls-based

variations have been developed for specialized applications. These variants include wear and scratch testing of hard surfaces (e.g., modified and unmodified inorganic materials [11-13], and mineralized biological tissues [9, 14]); friction and lateral force spectroscopy of biological surfaces [15-17]; force spectroscopy of inter- and intra-molecular interactions [18-22]; and measurement of viscoelastic behavior in synthetic polymers [23-26], inorganic media [27, 28], and biological systems [29-33]. In this review, we focus on the use of the nanoindentation method to measure spatial variations in the elastic properties of soft materials (e.g., synthetic polymer gels and biological tissues and cells). Evaluation of mechanical properties is an important component in the study of these diverse materials, and in subjects with size and handling constraints as typified by single cells, nanoindentation exists as the most viable method of obtaining absolute measures of basic physical quantities such as the elastic modulus. The suitability of the technique for detecting and quantifying inhomogeneities in biological samples is illustrated by Figure 2, in which the stiffness of a cartilage specimen is mapped along a line to reveal variations in the stiffness within the extracellular matrix and the presence of cells (low stiffness).

The nanoindentation of soft materials presents a set of challenges unique from the elastic-plastic deformation that is common when applying the technique to hard surfaces. AFM measurements, in particular, merit careful treatment due to the need to infer the load-indentation relationship from the position and deflection of the cantilever. With the AFM's ubiquity in fields from polymer science to the biomedical sciences as a tool for characterizing topographical and mechanical properties of biological and synthetic materials, a number of analysis methods have been developed for extracting elastic properties, namely Young's modulus (E) or the shear modulus (G), from the deflection-position data. These analysis methods are easily simplified for use with force-displacement data from depth-sensing systems. The aim of this paper is to help the reader select the appropriate procedure for determining the elastic response of soft materials using the AFM or DSN. We will first introduce the theoretical force-indentation models upon which the methods are based, followed by an explanation of how the models are cast into mathematical forms applicable to AFM and DSN data. Next, a number of common data-processing methods are reviewed. Details of a comprehensive algorithm that we developed for the automated extraction of Young's moduli from large collections of datasets are also presented, along with sample results. This is followed by a general discussion section that critically overviews the current state of the field, including the shortfall of more advanced interactive and nonlinear models. We conclude with a brief summary and commentary on future directions in the nanoindentation of soft materials.

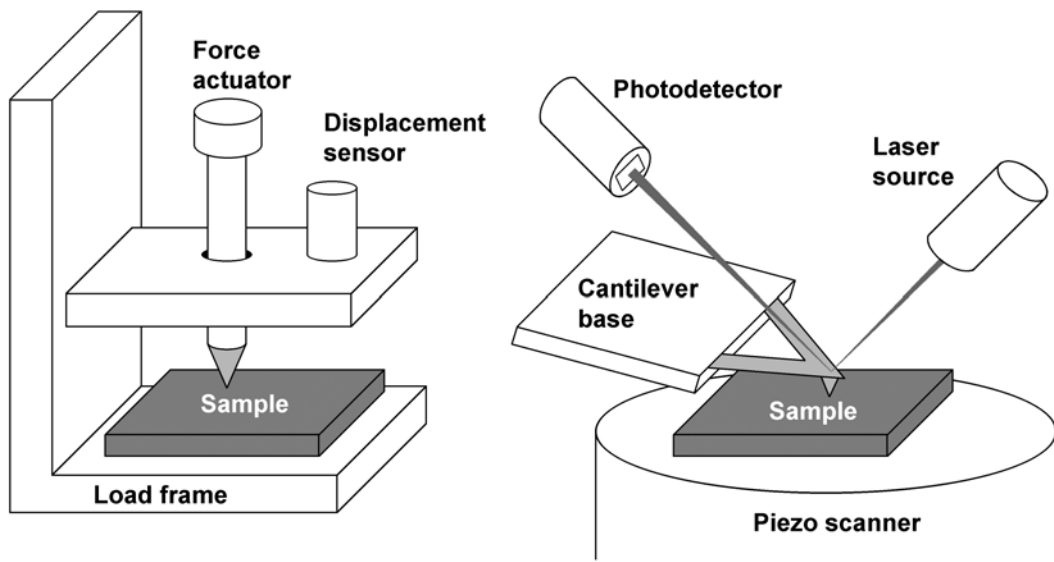


Figure 1. Schematics of the depth-sensing nanoindenter (left) and the atomic force microscope (right). The depth-sensing system can be load-controlled or displacement-controlled and allows precise measurement of both probe displacement and applied force. Force is usually generated through electrostatic actuation and displacement is usually measured using a capacitive sensor. In the atomic force microscope, displacement control is achieved by moving either the cantilever base or the sample, and force is inferred from laser-based measurements of cantilever deflection.

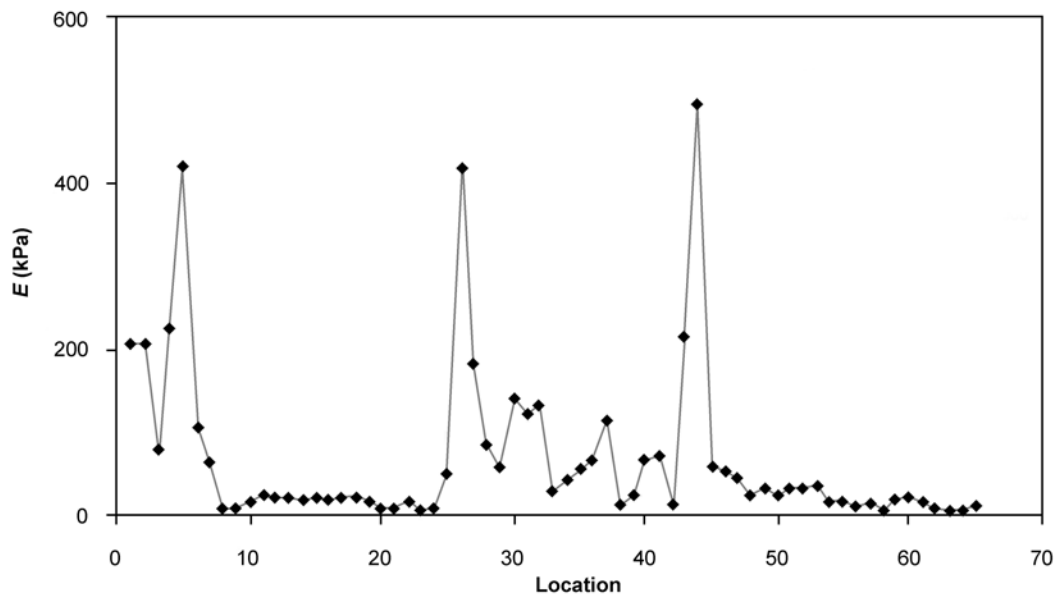


Figure 2. Young's modulus of a cartilage specimen as a function of position along a line [34]. The tissue was grown from chicken sternum chondrocytes seeded on a poly(vinyl alcohol) gel scaffold [35]. AFM indentations were performed approximately every 2.5 μm . Regions of very low stiffness are likely chondrocytes.

Review of mathematical models

Regardless of the type of instrument used in nanoindentation tests, extraction of elastic properties from the raw data entails the fitting of mathematical models of deformation behavior to the load-displacement (in the case of the DSN) or deflection-position data (in the case of the AFM). The models used are predominantly based on classic linear elasticity theory, with the fundamental conditions of material isotropy and homogeneity, infinitesimal indentation (i.e., small indentation depth and probe size in relation to sample size), and deformations that do not exceed the linear stress-strain regime. The seminal work in the field of contact mechanics is attributed to Hertz, who solved the problem of elastic contact between two ellipsoidal bodies [36]. The special case of indentation allows simplification of the contact problem to that of one between an elastic half-space and a rigid probe of well-defined geometry, first considered by Boussinesq [37] shortly following publication of Hertz's work. Numerous others (e.g., Love [38], Segedin [39], Landau and Lifshitz [40], and Sneddon [41]) have contributed to the theoretical framework to the point where exact solutions in the form of force-indentation relationships, contact pressure distributions, and stress and displacement fields are available for common axisymmetric geometries (e.g., cylinder, sphere, and cone).

When the indenter is spherical in shape, the resulting force-indentation relationship is often referred to as the Hertz equation. It is also common to refer to linear elastic contact as being "Hertzian." In their influential work published in 1971, Johnson *et al* [42] cited evidence of deviation from Hertzian behavior in the contact of elastic spheres. In the cited experiments, measured contact areas at small loads were considerably larger than predictions using the Hertz theory; at large loads, the deformations were Hertzian. They hypothesized that attractive surface forces were responsible for the considerable deviation from the Hertz prediction at small loads and modified the Hertz equation to account for the additional contribution to the force-indentation behavior. Derjaguin *et al* [43] formulated an alternative and apparently contradictory theory that led to debate over the accuracy of the two models [44]. The seeming inconsistency was resolved by Tabor [45], who identified the applicability of the two theories to opposite extremes of the relationship between sample compliance and the range of the adhesive force. Muller *et al* [46] and Greenwood [47] used the Lennard-Jones potential in their numerical analyses of interactions in the intermediate regime. Maugis [48] was able to consolidate the two theories in closed-form by deriving solutions of the relationship between force, contact radius, and indentation. The Maugis-Dugdale theory remains the most complete model of the influence of strong attractive surface energies on the contact of spheres that otherwise deform in a linearly elastic fashion.

Many exact and approximate methods of solution in the field of elasticity theory have been developed over the course of its rich history; detailed discussions of the methods can be found in texts on the subject (e.g., by Landau and Lifshitz [40], Johnson [49], and Barber [50]). In the following sections, we will summarize the simplified forms (i.e., applicable to the indentation of an elastic half-space by a rigid indenter) of the Hertzian solutions and the modified theories of Johnson *et al*, Derjaguin *et al*, and Maugis.

Hertzian indentation

Many solutions for indenter geometries commonly used in indentation can be represented by the generalized force-indentation relation:

$$F = \lambda \delta^\beta \quad (1)$$

where F is the force applied to the indenter, δ is the indentation depth, and the terms λ and exponent β are given in Table 1 along with the contact radius a for spherical (from the original Hertz theory) [36, 49], cylindrical [41, 51], sharp conical [10, 41, 51], and sharp square pyramidal [52] indenters. It is useful to define an elastic constant E^* of the indented sample:

$$E^* = 4E/(3(1-\nu^2)) \quad (2)$$

where E and ν are Young's modulus and Poisson's ratio of the sample, respectively. Poisson's ratio for common solids ranges from nearly 0 for cork to 0.5 for rubber-like materials whose volumes remain unchanged during deformation. Similar, approximate solutions for the pyramid were derived by Bilodeau [52] and by Rico *et al* [33]. The Bilodeau solution more accurately represents the geometry of contact by a square while the solution of Rico *et al* utilizes an effective circle of the same area. Various terms describing the taper geometry of cones and pyramids are encountered in the literature (e.g., tip angle, opening angle, and included angle are all equivalent while semivertical angle and incline angle both refer to the complement of the tip angle). To minimize confusion arising from the terminology, we will use the tip angle 2ϕ to describe both cones and square pyramids, where ϕ is complementary to the incline angle θ of the faces of the pyramid as shown in Figure 3. For conical and pyramidal indenters with blunted (i.e., rounded) tips of radius R , Equation (1) does not apply. Rather, force and indentation are related by the equations [33, 51, 53]

$$\begin{aligned} F = & \frac{3E^*}{2} \left\{ a\delta - m \frac{a^2}{\tan \phi} \left[\frac{\pi}{2} - \arcsin \left(\frac{b}{a} \right) \right] - \frac{a^3}{3R} \right. \\ & \left. + (a^2 - b^2)^{1/2} \left[m \frac{b}{\tan \phi} + \frac{a^2 - b^2}{3R} \right] \right\} \end{aligned} \quad (3)$$

$$\delta + \frac{a}{R} [(a^2 - b^2)^{1/2} - a] - n \frac{a}{\tan \phi} \left[\frac{\pi}{2} - \arcsin \left(\frac{b}{a} \right) \right] = 0 \quad (4)$$

where b is the radius at which the tapered sides transition into a spherical tip and m and n are constants with specific values for the cone ($m = 1/2$, $n = 1$) and the pyramid ($m = 2^{1/2}/\pi$, $n = 2^{3/2}/\pi$). Again, the solution of Rico *et al* for the blunt pyramid is based on an effective circular contact area of radius a . For both conical and pyramidal profiles, the corresponding sharp-tipped solutions are recovered when $R = b = 0$ while the limiting case of $R \rightarrow \infty$ yields solutions for truncated (i.e., flat-ended) tips.

Table 1. Terms of the generalized force-indentation relation and contact radii for various models.

Model	λ	β	a
Hertz: sphere of radius R	$E * R^{1/2}$	$3/2$	$(R\delta)^{1/2}$
Flat cylinder of radius r	$3E * r / 2$	1	r
Sharp cone of tip angle 2ϕ (see Figure 3)	$\frac{3E * \tan \phi}{2\pi}$	2	$\frac{2\delta \tan \phi}{\pi}$
Sharp pyramid of tip angle 2ϕ and incline angle θ (see Figure 3): Bioldeau solution [52] [†]	$1.4906 \frac{3E * \tan \phi}{8}$	2	$\frac{1.579^{1/2} \delta \tan \phi}{2}$
Rico <i>et al</i> solution [33] [‡]	$\frac{3E * \tan \phi}{2^{5/2}}$	2	$\frac{\delta \tan \phi}{2^{1/2}}$

$E^* = 4E / 3(1 - \nu^2)$, where ν is Poisson's ratio and E is Young's modulus

[†] Contact radius is actually half the length of one side of the square area of contact

[‡] Effective contact radius is of a circle with equal contact area

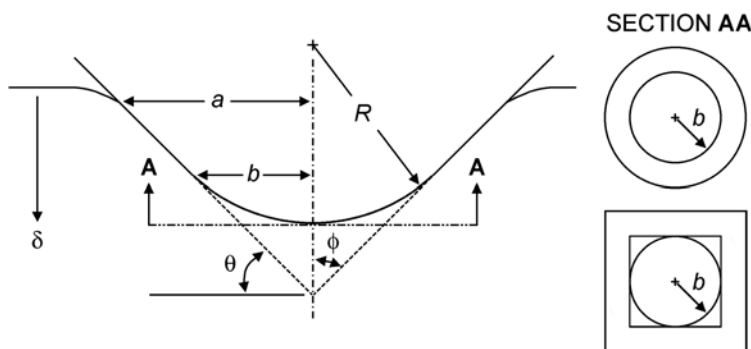


Figure 3. Geometry of blunt and sharp conical and pyramidal tips. The dimension $2a$ is the diameter of the circle of contact for the cone and the length of one side of the square of contact for the pyramid. The blunt tips transition at radius or half-width b to a round tip with radius R . For a smooth transition, $b = R\cos\phi$. The incline angle of the faces of the pyramid is represented by θ .

Adhesion-influenced indentation

It is constructive to start with the distinction often made between the terms “attraction” and “adhesion.” The former term is used to refer to the interactions between two surfaces as they are brought within close proximity to each other prior to contact while the latter term refers to the resistance to separation as two contacting surfaces are pulled apart [54]. Because the theories presented here are concerned solely with the maximum force of interaction, we will henceforth dispense with the convention and use the terms “adhesive force” and “adhesion” exclusively. The incorporation of adhesive forces into contact mechanics was pioneered by Johnson *et al* [42], who were motivated by a large body of evidence suggesting the existence of such forces between both hard and rubber-like solids. The well-known JKR (Johnson-Kendall-Roberts) theory makes use of the apparent Hertz load, or the equivalent load in the absence of adhesive forces that produces the enlarged contact area. Adopting the notation of Pietrement and Troyon [55], in which subscripts in parentheses, e.g., (JKR) are used to differentiate between different theories whenever ambiguity is likely, the JKR theory can be expressed by the following equations [42, 55]:

$$\delta = \frac{a_{(JKR)}^2}{R} - \frac{4}{3} \sqrt{\frac{a_{(JKR)} F_{ad(JKR)}}{RE^*}} \quad (5)$$

$$a_{(JKR)} = \left[\frac{R}{E^*} \left(\sqrt{F_{ad(JKR)}} + \sqrt{F_n + F_{ad(JKR)}} \right)^2 \right]^{1/3} \quad (6)$$

$$F_{ad(JKR)} = (3/2)\pi\gamma R \quad (7)$$

where F_n is the applied normal force, F_{ad} is the characteristic adhesive or pull-off force between the two surfaces that is assumed to exert a constant influence while the surfaces are in contact, and γ is the interfacial energy. Note that interfacial energy has units of energy per unit area (e.g., J/m²). At the point of contact or separation, when $F_n = -F_{ad}$, the indentation is

$$\delta_{0(JKR)} = -\frac{1}{3} \frac{F_{ad(JKR)}}{(E^*)^{2/3} R^{1/3}}^{2/3} \quad (8)$$

and the contact radius is the nonzero quantity

$$a_{0(JKR)} = (RF_{ad}/E^*)^{1/3} \quad (9)$$

Equations (8) and (9) emphasize the chief consequences of the JKR theory, namely that initial contact or pull-off occurs abruptly once $F_n = -F_{ad}$ and that indentations are negative over the range $-F_{ad} \leq F_n \leq -(8/9)F_{ad}$ [56]. Note that F_n is also negative over this range (i.e., the tip is being “pulled by” rather than

“pushed into” the sample). A negative indentation can be interpreted as deformation of the sample surface *towards* the probe (i.e., opposite in direction to the deformation due to Hertzian indentation). The JKR theory is therefore suitable for modeling interactions between the tip and a very compliant sample, in which the adhesive force is strong enough to overcome the sample stiffness and cause the surface to be drawn towards the tip.

In forming the DMT (Derjaguin-Muller-Toporov) theory, Derjaguin *et al* [43] assumed that the deformed surface profile obeys the Hertz model. The relevant expressions are

$$\delta = a_{(DMT)}^2 / R \quad (10)$$

$$a_{(DMT)} = \left[\frac{R}{E^*} (F_n + F_{ad(DMT)}) \right]^{1/3} \quad (11)$$

$$F_{ad(DMT)} = 2\pi\gamma R \quad (12)$$

Note from Equation (10) that the contact radius matches that for the Hertz model given in Table 1 and that the applied force-indentation relationship is essentially the Hertz relationship with the addition of the adhesive force term. Consequently, in contrast to the JKR theory, the minimum indentation is zero and the contact area vanishes at zero indentation depth (i.e., when $F_n = -F_{ad}$, $\delta = a = 0$).

The sharp differences between the JKR and DMT theories instigated the debate that was finally settled by Tabor, who defined a relationship between the range of the surface forces and the compliance of the sample [45]. The JKR theory was shown to be valid for indentation involving a relatively compliant material, an indenter of large tip radius, and strong adhesive force. The DMT theory was found to apply to the opposite extreme of the relationship between the three parameters (i.e., stiff material, small tip radius, and weak adhesive force). Using numerical methods, Muller *et al* [46] and Greenwood [47] investigated the relationship in the intermediate regime by adapting the Lennard-Jones potential to model the adhesive surface interactions as a function of separation distance. The lack of a closed form solution in the intermediate regime was overcome by Maugis [48], whose solution employed the Dugdale potential (a square well approximation of the Lennard-Jones potential; see Figure 4). Maugis also defined a nondimensional parameter λ to represent the relationship between sample compliance, tip radius, and adhesive force first addressed by Tabor [48, 55]:

$$\lambda = 2\sigma_0 \left[\frac{R}{\pi(E^*)^2 \gamma} \right]^{1/3} \quad (13)$$

where σ_0 is the maximum adhesive force in the Dugdale potential. It is assumed that σ_0 exerts an influence over an area of radius c that is greater than the actual contact radius a . Regions of applicability of the DMT and JKR models are defined by $\lambda < 0.1$ (i.e., weak adhesive force and small tip radius relative to sample compliance) and $\lambda > 5$ (strong adhesive force and large tip radius relative to sample compliance), respectively. The solution, known as the Maugis-Dugdale (MD) theory, is given by [48, 55]

$$\frac{\lambda \bar{a}^2}{2} \left[(m^2 - 2) \tan^{-1} \sqrt{m^2 - 1} + \sqrt{m^2 - 1} \right] + \frac{4\lambda^2 \bar{a}}{3} \left[\sqrt{m^2 - 1} \tan^{-1} \sqrt{m^2 - 1} - m + 1 \right] = 1 \quad (14)$$

$$\bar{F}_n = \bar{a}^3 - \lambda \bar{a}^2 \left[\sqrt{m^2 - 1} + m^2 \tan^{-1} \sqrt{m^2 - 1} \right] \quad (15)$$

$$\bar{\delta} = \bar{a}^2 - \frac{4\lambda \bar{a}}{3} \sqrt{m^2 - 1} \quad (16)$$

where $m = c/a$ and the contact radius, applied and adhesive force, and indentation have the nondimensionalized forms

$$\bar{a} = a \left(\frac{E^*}{\pi \gamma R^2} \right)^{1/3} \quad (17)$$

$$\bar{F} = \frac{F}{\pi \gamma R} \quad (18)$$

$$\bar{\delta} = \delta \left[\frac{(E^*)^2}{\pi^2 \gamma^2 R} \right]^{1/3} \quad (19)$$

Use of the MD theory is complicated by the indirect relationship between force and indentation. Carpick *et al* [57] sought to enhance the tractability of the MD model by developing an empirical approximation of the relationship between contact radius and applied force. The Carpick-Ogletree-Salmeron (COS) equation is given by [55, 57]

$$\frac{a}{a_{0(\alpha)}} = \left(\frac{\alpha + \sqrt{1 + F_n / F_{ad(\alpha)}}}{1 + \alpha} \right)^{2/3} \quad (20)$$

where $a_{0(\alpha)}$ is the contact radius at zero applied force and α is a nondimensional parameter related to λ by

$$\lambda = -0.924 \ln(1 - 1.02\alpha) \quad (21)$$

The subscript (α) distinguishes the equation as an empirical form of the MD model and the limits of α are 0 for the DMT case and 1 for the JKR case. Utilizing the same approach, Pietrement and Troyon generated a force-indentation relationship that deviates from the MD model by 1% or less. The Pietrement-Troyon (PT) equation is [55]

$$\delta = \frac{a_{0(\alpha)}^2}{R} \left[\left(\frac{\alpha + \sqrt{1+F_n/F_{ad(\alpha)}}}{1+\alpha} \right)^{4/3} - S_{(\alpha)} \left(\frac{\alpha + \sqrt{1+F_n/F_{ad(\alpha)}}}{1+\alpha} \right)^{\frac{2}{3}\beta_{(\alpha)}} \right] \quad (22)$$

The relationship between α and λ is now given by

$$\lambda = -0.913 \ln(1 - 1.018\alpha) \quad (23)$$

and the terms $a_{0(\alpha)}$, $F_{ad(\alpha)}$, $\beta_{(\alpha)}$, and $S_{(\alpha)}$ are functions of α given by

$$\bar{a}_{0(\alpha)} = -0.451\alpha^4 + 1.417\alpha^3 - 1.365\alpha^2 + 0.950\alpha + 1.264 \quad (24)$$

$$\bar{F}_{ad(\alpha)} = 0.267\alpha^2 - 0.767\alpha + 2.000 \quad (25)$$

$$S_{(\alpha)} = -2.160\alpha^{0.019} + 2.7531\alpha^{0.064} + 0.073\alpha^{1.919} \quad (26)$$

$$\beta_{(\alpha)} = 0.516\alpha^4 - 0.683\alpha^3 + 0.235\alpha^2 + 0.429\alpha \quad (27)$$

where the nondimensionalized forms of $a_{0(\alpha)}$ and $F_{ad(\alpha)}$ are defined by Equations (17) and (18). The COS and PT equations provide the means to effectively apply the MD model to experimental data.

The JKR, DMT, and MD theories all apply to spherical indenters. Based on methods developed in the field of fracture mechanics and a modified JKR model attributed to Maugis [58], Sun *et al* derived the following adhesive contact model for hyperboloid (blunted conical) indenters [59]:

$$\delta = \frac{aA}{2R} \left[\frac{\pi}{2} + \arcsin \frac{(a/A)^2 - 1}{(a/A)^2 + 1} \right] - \left(\frac{8\pi a \gamma}{3E^*} \right)^{1/2} \quad (28)$$

$$F_n = \frac{3E^*}{2} \left\{ \frac{A}{2R} \left[aA + \frac{a^2 - A^2}{2} \left[\frac{\pi}{2} + \arcsin \frac{(a/A)^2 - 1}{(a/A)^2 + 1} \right] \right] - a \left(\frac{8\pi a \gamma}{3E^*} \right)^{1/2} \right\} \quad (29)$$

where $A = R \cot(\phi)$.

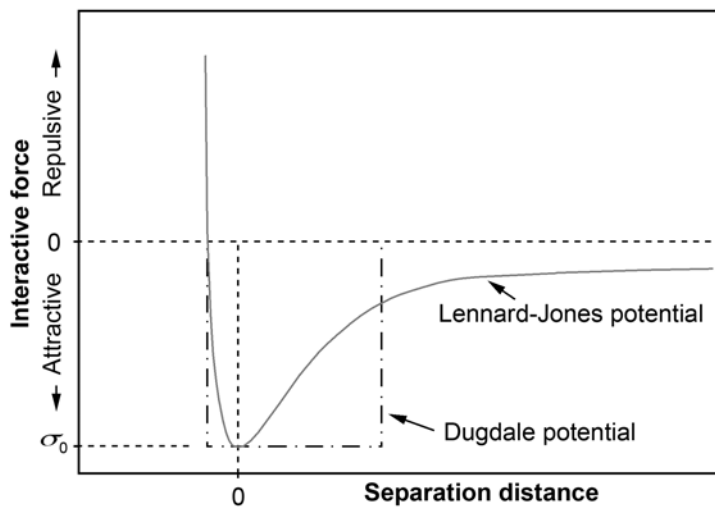


Figure 4. Force-separation laws based on the Lennard-Jones potential and the Dugdale square-well potential. In the contact mechanics theories, maximum adhesive force ($\sigma_0 = F_{ad}$) occurs at the point of contact or separation (zero separation distance).

Treatment of AFM and DSN Data

The types of raw data obtained from DSN and AFM indentation tests differ significantly. By virtue of its force actuation, the DSN provides a much more direct measurement of the force-indentation behavior, requiring only the identification of a displacement reference point in the force-displacement data. In the AFM, neither force nor indentation depth are measured directly – force is a function of the deflection of the cantilever while indentation depth is a function of both the cantilever deflection and the displacement of the cantilever base. It should therefore be noted that the common use of the terms “force-displacement curve” and “force curve” in referring to AFM nanoindentation data is technically incorrect. In this section, we cover the essential reference points that are necessary in converting the raw data to force-indentation relationships. Although these characteristic points exist in both extension and retraction curves, we will use terminology commonly associated with extension curves (e.g., “contact” instead of “separation”) to minimize confusion.

Essential reference points in AFM data

It is important to define a sign convention for the cantilever deflection (d), the position of the fixed end or base of the cantilever (z), and the indentation δ . The adopted convention is shown in the first row of Figure 5. Note that z increases continually (usually in a linear manner) during tip extension stroke and returns to its initial value at the end of the retraction stroke. Also shown schematically in Figure 5 is the relationship between d , δ , and the contact

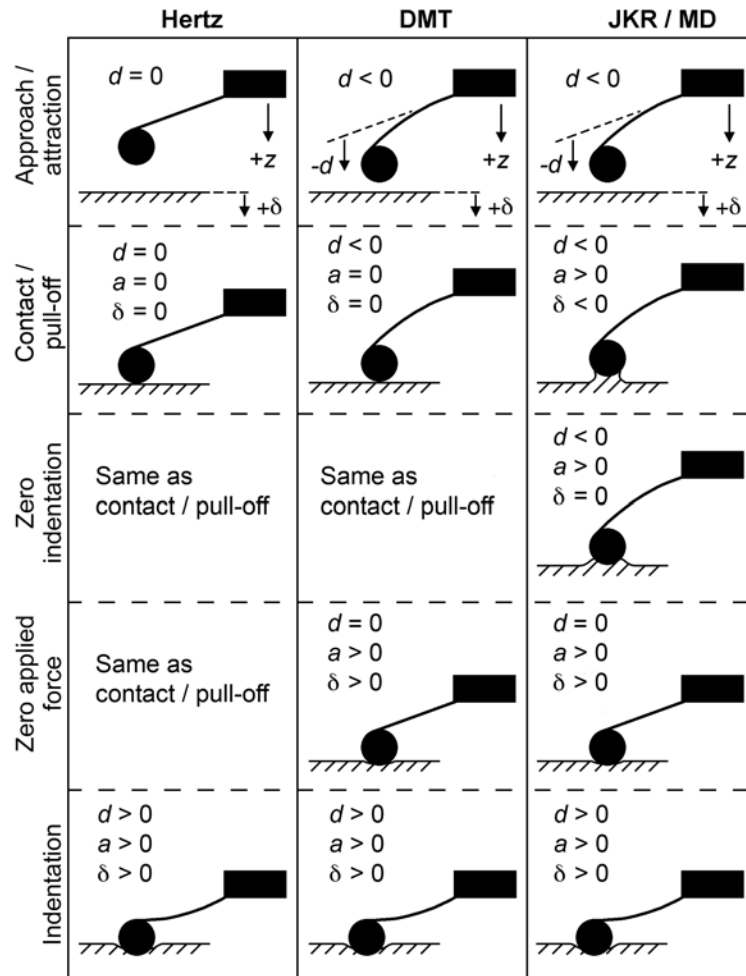


Figure 5. Schematic of AFM cantilever deflection (d), cantilever base displacement (z), indentation (δ), and contact radius (a) as predicted by the Hertzian, DMT, JKR, and MD theories during the indentation process. The sign convention is as follows: cantilever base displacement towards the sample surface is positive; convex bending of the cantilever (deflection d in direction of piezo motion) is negative; and convex deformation of the sample surface δ (initial contact or pull-off in the JKR and MD theories) is also negative.

radius a at each reference point. The corresponding d vs. z curves for the various models are displayed in Figure 6. Starting with the cantilever deflection as a function of the position of the cantilever, the indentation δ is defined by [34, 56, 60]

$$\delta = (z - z_0) - (d - d_0) = (z - d) - (z_0 - d_0) = w - w_0 \quad (30)$$

where the reference point (z_0, d_0) is the point of zero indentation. The transformed variable $w = z - d$ and its value at the reference point, w_0 , are introduced for simplification. The indentation reference point is shown in Figure 6 for Hertzian

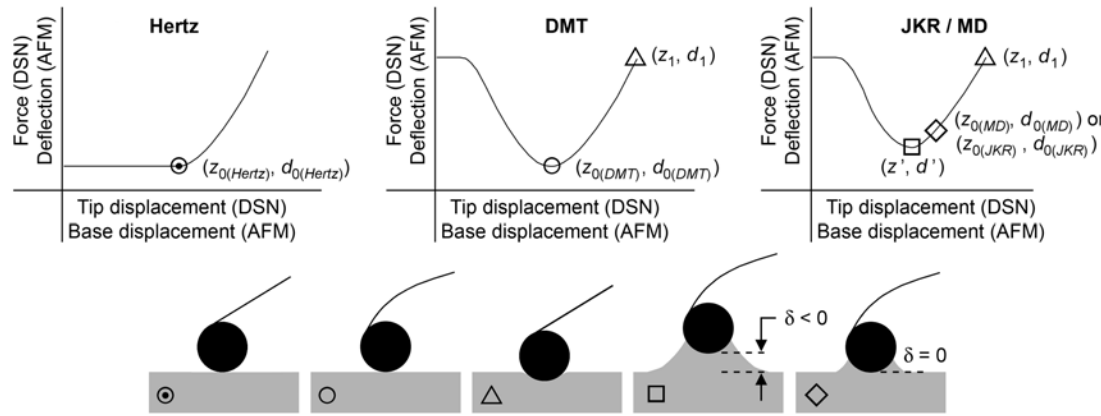


Figure 6. Comparison of force-displacement behavior in Hertzian and adhesive contact models. Raw data for the DSN is in the form of applied force vs. tip displacement. For the AFM, raw data is in the form of cantilever deflection (d) vs. displacement of the cantilever base. Tip displacement and cantilever base displacement are mathematically equivalent and both designated by z . Indentation is always zero at the point of contact in the Hertzian (indicated by \odot) and DMT (indicated by \circ) models, but can be negative in the JKR and MD models (indicated by \square) to allow for deflection of the sample surface towards the tip. Equally important in the JKR and MD models is the point of zero indentation (indicated by \diamond), which is the reference point used to calculate indentation depth from the force-displacement data. In all adhesive contact theories, the point of zero applied force (i.e., zero cantilever deflection, indicated by \triangle) occurs at positive indentation depth.

and adhesive models. The applied force is directly related to the deflection through the spring constant of the cantilever (k_c) by

$$F_n = k_c(d - d_1) \quad (31)$$

where d_1 is the zero-deflection position of the cantilever. Note the distinction between the point of zero external force (z_1, d_1) and the indentation reference point (z_0, d_0); the two points are coincident only in Hertzian mechanics. All reference points can be expressed in terms of z or w ; we will use them interchangeably. Substitution of Equations (30) and (31) into the contact mechanics models casts the models into AFM-specific forms. For example, Equation (1) becomes

$$k_c(d - d_1) = \lambda(w - w_0)^\beta \quad (32)$$

where $d_1 = d_0$ for the Hertzian models.

In the DMT model, both indentation depth and contact radius are zero at the point of contact (z_0, d_0) and increase with the externally applied load following Equation (10). In physical terms, the cantilever is permitted to

deflect toward the sample surface prior to contact, reaching its maximum *negative* deflection or maximum adhesive force at the point of contact (see Figure 5 and Figure 6). At the onset of contact in the JKR and (to a lesser extent) MD models, the tip and sample surface are instantaneously drawn together, resulting in a nonzero contact radius and negative indentation depth. The contact point in the JKR and MD models is denoted by (z', d') in Figure 6. As in the DMT theory, contact occurs at the maximum adhesive force F_{ad} .

Indentation reference in DSN data

As mentioned previously, the DSN measures the displacement of the tip in response to an applied force. Since the applied force is always known, the zero-force reference points shown in Figure 6 are no longer necessary. Compared to AFM data, the indentation takes on the much simpler form

$$\delta = (z - z_0) \quad (33)$$

where z_0 is now the tip displacement at the point of zero indentation. In the Hertzian and DMT models, z_0 also corresponds to the point of contact. This is not the case when applying the JKR and MD theories, where the indentation is negative at the point of contact (z' in Figure 6).

Application of mathematical models to experimental data

The fundamental challenge in the processing of AFM and DSN raw data for the purpose of extracting *absolute* elastic properties is the accurate identification of all essential reference points. Summarized in Table 2 are the reference points required for the possible combinations of instrument type (DSN or AFM) and the governing theory (Hertzian, DMT, JKR, and MD). The frequent use of Hertzian models in the processing of AFM data by researchers has led to a number of common techniques for identifying the contact point (z_0, d_0) . We therefore devote the next section to the discussion of some of these methods, which are readily simplified for the processing of DSN datasets. Reference point independent methods such as the work-based approach of A-Hassan *et al* [61] are practical when only relative measures of elasticity are desired, and will not be included in the discussion. Also excluded is the method developed by Oliver and Pharr [62], which is suitable for analyzing data from the indentation of materials stiff enough that the compliance of the indenter must be considered.

Virtually all of the analysis methods to be discussed entail regression analysis whereby an appropriate contact mechanics model is fit to the data, either concurrent with or subsequent to identification of the reference points. When applying the Hertzian models, a viable alternative to the optimization-based

Table 2. Essential reference points in the processing of AFM and DSN data.

Hertz		DMT	JKR / MD
DSN	Contact: z_0	Contact: z_0	Contact: z' Zero indentation: z_0
AFM	Contact: (z_0, d_0)	Contact: (z_0, d_0) Zero force: (z_1, d_1)	Contact: (z', d') Zero indentation: (z_0, d_0) Zero force: (z_1, d_1)

approach is a point-by-point computation of Young's modulus once the location of the contact point has been established [60]. Rather than fitting the contact model to the dataset, the point-wise approach is implemented by directly solving for E at each point in the contact region. The value of Young's modulus can then be averaged over the interval in which it remains most stable. It is not advisable to evaluate the mean over the whole region due to high levels of noise in the vicinity of the contact point and possible nonlinearities such as strain hardening at large indentation depths.

In measuring elastic moduli, Poisson's ratio of the probed material must be known (i.e., in the regression analysis, E is treated as a fitting parameter and ν is a constant). At the loading rates and length scales typical of the nanoindentation of biological and synthetic rubberlike materials, the effects of exudation and imbibition of fluid are negligible and the assumption of incompressibility ($\nu = 0.5$) is usually valid [34, 63, 64].

Contact point identification methods for Hertzian analysis of AFM data

Approaches to contact point identification can be classified as being constrained or unconstrained [34]. The constrained approaches restrict the contact point to be a member of the set of (z, d) data pairs while the unconstrained methods permit the contact point to lie off the data curve. Because an incorrectly identified contact point will bias the fitting of the mathematical models to the data, constrained methods should be avoided when levels of noise in the data are high. Manually selecting the contact point based on visual inspection of the data curve is the simplest constrained approach [60]; the method has largely been abandoned due to its high degree of subjectivity. Nyland and Maughan [65] devised a more objective constrained method using the first and second derivatives of the cantilever deflection with respect to the cantilever base displacement. After smoothing the data curve, the data point corresponding to the maximum value of the second derivative or to the extrapolated point of zero first derivative is chosen as the contact point. For probing very soft materials in which the cantilever deflection is small, even small levels of noise can greatly affect calculations of the derivatives and

introduce large errors. Since various tip-sample interaction forces emerge at short separation distances and continue to exert an influence at the onset of contact, the data in this region are usually the noisiest [60]. Hence, the second derivative method is limited in its applicability.

Jaasma *et al* [66] formulated a derivative-based approach that improves on the method of Nyland and Maughan by evaluating data from the contact region, thereby eliminating bias from the high levels of noise and nonlinearity associated with the vicinity of the contact point. Substituting Equations (30) and (31) into Equation (1) and then differentiating with respect to w yields

$$\frac{\partial d}{\partial w} = \frac{\beta\lambda}{k_c} (w - w_0)^{\beta-1} \quad (34)$$

It is evident that the derivative is zero at the point of contact or separation. To find w_0 , the procedure requires fitting Equation (34) to the derivative of the data in some predefined range (e.g., Jaasma *et al* used for one range 10-40% of the extreme value of $\partial d/\partial w$) using the appropriate terms from Table 1 and then extrapolating the equation to $\partial d/\partial w = 0$. The corresponding data point is selected as the point of contact or separation.

In sequential or linear search schemes, the point that produces the best least squares fit of the indentation data is selected as the contact point. The derivative and visual inspection methods generate comparatively poorer fits because the contact point in those non-iterative methods is determined without considering its effect on the quality of fit. We identified three variations of sequential search based on the constraints [34]. The constrained variation is best suited for data with low levels of noise because it selects the contact point from among the collected dataset. Dimitriadis *et al* [60] employed this variant to demonstrate that selection of the contact point by visual inspection produces fits that may differ significantly from those obtained by objectively selecting the best contact point through a methodical search procedure.

In the semi-constrained variation of sequential search, the z -coordinate at each iteration is chosen from the acquired z -position vector and the corresponding d_0 along with E are the fitting parameters. Finally, neither z_0 nor d_0 is fixed in the unconstrained variant of the fitting procedure. Rather, the (z, d) pair is used as the initial guess in the regression analysis. In a non-iterative scheme proposed by Radmacher *et al* [32, 67], d_0 is estimated by averaging the range of d values over the non-contact region, leaving z_0 and Young's modulus E as the fitting parameters. This approach can be considered the semi-constrained counterpart to the visual inspection method and is likewise prone to error when noise levels are high.

Kolambkar [68] formulated a more rigorous unconstrained approach by evaluating the error associated with assuming an incorrect contact point. He expanded the resulting force-indentation relation in a power series in $(d^+ - d_0)$, where d^+ is the d - coordinate of an assumed contact point (z^+, d^+) chosen by visual inspection. Neglecting higher order terms, the expansion yields

$$k_c(d - d^+) \approx \lambda(w - w^+)^{\beta} + \beta\lambda^{\beta-1/\beta} k_c(d^+ - d_0)^{1/\beta} (w - w^+)^{\beta-1} \quad (35)$$

which can be fit to the dataset to obtain w_0 (or z_0), d_0 , and E . A major disadvantage of the power series methods is that they are extremely sensitive to the inclusion of data from the non-contact region (i.e., attempting to fit contact mechanics models to a dataset that contains a substantial number of points from the non-contact region will weaken the fit of the contact portion). Although Kolambkar recommends disregarding the points prior to (z^+, d^+) , this approach is only practicable in cases where the location of the contact point is easily discernible by visual inspection.

The methods discussed thus far all require the contact point to be bracketed by the endpoints of the dataset (i.e., the “ramp” size, $0 < z_0 < z_{\max}$, where z_{\max} corresponds to the point of maximum indentation). In certain instances, however, the contact point may not be captured within the dataset or may be situated in a portion of the data that exhibits non-Hertzian behavior. The former condition is most likely to occur in the indentation of very soft materials, where the cantilever deflection at the onset of contact may not be discernible from the real-time deflection vs. piezo displacement (d vs. z) plot. Consequently, it may be difficult to determine an appropriate ramp starting position that brackets the contact point. The latter condition is usually attributable to the existence of non-adhesive tip-sample interactions. Such interactions, for which no contact mechanics theories have been developed, present an ill-defined complication – the contact point may be situated in a portion of the curve that exhibits nonlinearity. Elimination of such data by truncation will result in the exclusion of the contact point from the retained dataset. We introduced a backwards search scheme [34] that allows fitting of such previously intractable datasets. The method utilizes the semi-constrained sequential search method. At each step, the value of the assumed z_0 from the previous iteration is decremented by the z -spacing in the original data. The search is halted once no further improvement to the least squares fit of the retained data is detected.

Approaches for dealing with adhesion

In comparison to Hertzian analysis methods, there exist relatively few approaches based on adhesive contact theories. Pietrement and Troyon outlined a general procedure for applying the PT equation [55], but assumed

the raw data to be in the form of force and indentation depth. Sun *et al* [59] used the JKR theory as the starting point of a method based on the region of adhesion-induced indentation (i.e., from the point of contact to the zero-force reference). By selecting two points from this region (e.g., the zero-force reference and the contact point) and applying Equations (5) and (6) or Equations (28) and (29), depending on the tip geometry, to both points, a system of four equations with four unknowns (the two contact radii, the interfacial energy γ , and Young's modulus E) is obtained. Use of this method requires first converting the raw data to values of force and indentation, and hence subjective selection of the essential reference points.

Cao *et al* [69] developed a technique for analyzing DSN data based on the determination of the shift in the applied force at the point of zero indentation; in the absence of adhesive forces, the points of contact, zero indentation, and zero force are coincident, as discussed previously. In essence, the method requires subjective selection of the indentation reference point and transformation of the data using a relationship similar to Equation (33). The transformed data can be fit with the JKR, DMT, or PT equations.

We developed an approach that eliminates manual and subjective identification of the essential reference points in AFM data [56]. The zero-force reference point (z_1, d_1) and point of contact (z', d') are established from conspicuous features of the d vs. z curve while the indentation reference point is found by an unconstrained search using the PT equation. The procedure is summarized in the Appendix.

Automated processing of large collections of data

Software controlled, high-resolution nanoindentation probing (often referred to as “force mapping” or “force-volume mapping”) using the AFM or DSN equipped with precise scanning capability has made large-scale mechanical measurements using these instruments possible. However, robust data processing methods are required to fully realize the high-throughput potential. The majority of automated methods are based on Hertzian mechanics and therefore inadequate for processing datasets that exhibit adhesive behavior. Of these methods, the most robust is perhaps the relative method developed by A-Hassan *et al* [61], which eliminates uncertainties associated with identifying the contact point but is of limited practicality when compared to absolute approaches. A number of studies have demonstrated the values of absolute approaches (e.g., the ability to compare measurements with those obtained using other methods). Radmacher and his colleagues used their non-iterative, semi-constrained search scheme in mapping the elastic modulus of various cells [32, 67, 70, 71]. Jaasma *et al* likewise applied their objective, derivative-based method in the automated processing of data obtained from the indentation of osteoblast and fibroblast cells [66, 72] while Haga *et al* [73] automated the

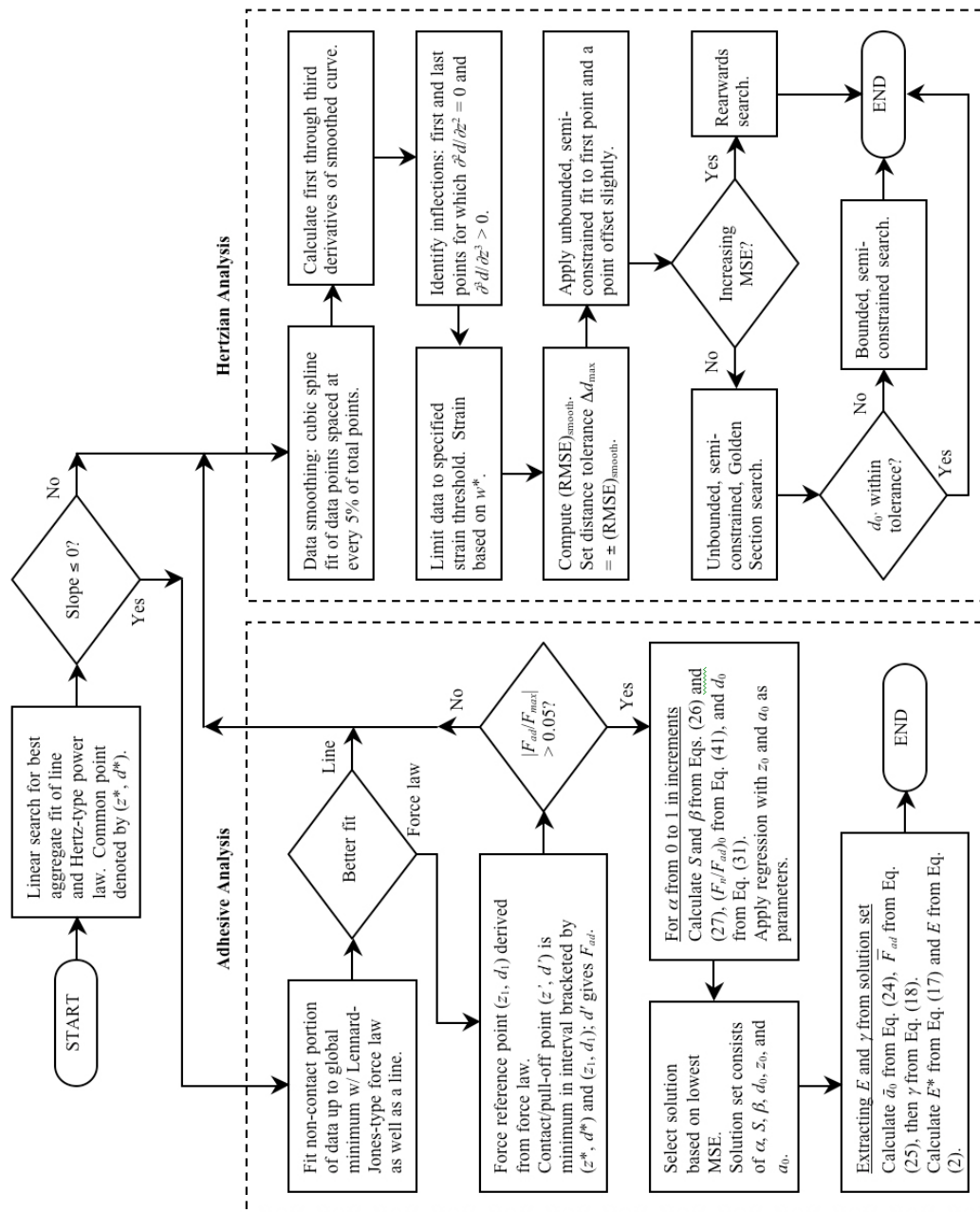


Figure 7. Flowchart representation of the comprehensive algorithm for the extraction of Young's moduli from AFM nanoindentation data

derivative method of Nyland and Maughan in probing the elastic modulus of fibroblasts. Finally, Nitta *et al* [74] used least-squares curve fitting of the Hertz model in generating elastic modulus maps of a polymer gel.

The use of a single objective approach in an automated fitting routine does not guarantee consistency in producing acceptable results because each approach has deficiencies with respect to certain types of datasets [34]. A comprehensive scheme for extracting elastic properties from indentation data must be capable of detecting the presence of significant adhesive forces and applying the appropriate contact mechanics model regardless of the location of the contact point. It must also incorporate strategies for handling contingencies such as excessive noise or tip-sample repulsive effects in the vicinity of the point of contact. We present here an algorithm, shown in flowchart form in Figure 7, which integrates a number of synergistic strategies to maximize the capability to process previously intractable or problematic datasets. Although presented in the context of processing AFM data, this procedure can be simplified for DSN data with relative ease.

The comprehensive scheme of Lin *et al*

A cursory fitting process is first performed to determine whether significant adhesive interactions are present. Using Step 2 in the Appendix, the slopes of the two sets of linear fits are evaluated to determine the presence of adhesive forces: if both slopes are positive, Hertzian analysis is performed; otherwise, if either or both slopes are negative, analysis is conducted using the PT equation by following the procedure outlined in the Appendix with the order of Steps 1 and 2 reversed.

The Hertzian analysis is summarized in Steps 1-6 below:

1. A data smoothing routine using cubic splines is performed to identify and trim spurious portions of the curve. Alternative smoothing methods (e.g., low pass filtering) may be applied. From the smoothed curve, first order ($\partial d/\partial w$) through third order derivatives are obtained. Inflection points are then identified by evaluating second and third derivatives along the curve (e.g., a zero of the second derivative with a corresponding positive third derivative is an upturn in the curve). Convex inflections near the beginning of the curve are indicative of non-adhesive tip-sample interactions while nonlinearities due to experimental factors (e.g., use of a cantilever of insufficient stiffness, sample defects such as rigid inclusions, and contribution from the underlying substrate caused by small sample thickness) may be revealed by inflections near the point of maximum cantilever deflection. In Figure 8, examples of both types of behavior are shown. This preprocessing step attempts to identify and remove contributions from such nonlinear effects.
2. After truncating the dataset, nonlinearities caused by material-dependent phenomenon such as strain hardening and softening may still exist. If the

strain threshold at which the linear assumption breaks down is known, it can be used to further limit the range of data to be analyzed. For a spherical indenter, the normal strain ε_{zz} is [60]

$$\varepsilon_{zz} = \frac{2a}{\pi R(1-\nu)} \quad (36)$$

where the contact radius a from Table 1 is $(R\delta)^{1/2}$. The point (w^*, d^*) from Step 2 of the Appendix is used as an approximate contact point in determining the position w_{lim} at which the specified strain limit ε_{lim} occurs. Substituting Equation (30) into Equation (36) with w^* in place of w_0 ,

$$w_{lim} = w^* + \left[\frac{\pi \varepsilon_{lim} R^{1/2} (1-\nu)}{2} \right]^2 \quad (37)$$

3. The level of noise in the data is determined by computing the root-mean square-error (RMSE) of the smoothed fit from Step 1. This value, which we denote by $(RMSE)_{smooth}$ is used to define the *distance tolerance*, or an upper bound of allowable deviation of the contact point from the original data curve. This tolerance is defined by $\Delta d_{max} = \pm(RMSE)_{smooth}$.
4. The unbounded, semi-constrained sequential search procedure is implemented. Using the mean-square-error (MSE) as a measure of goodness-of-fit, points from the beginning of the retained data to the current assumed contact point are fitted with a straight line while the remaining points are fitted with the appropriate contact model. The linear fit is necessary to maintain consistency in the total number of data points; goodness-of-fit measures are prone to improve as the size of the dataset decreases. A full search is not necessary. Instead, compare the MSE of the first point (minimum z) with that of a point offset by a small distance. If the contact point is bracketed by the endpoints of the retained dataset, the MSE will be a smooth, unimodal function of the position of the assumed contact point and the MSE of the first point will be larger (Condition 1). Otherwise, the MSE exhibits an initially increasing trend with the assumed z_0 (Condition 2).
5. For Condition 1, a Golden Section search for the minimum MSE is applied to find a viable contact point. If this point does not exceed the distance tolerance, no further processing is necessary. Otherwise, a bounded semi-constrained search is performed in the point. A spread of roughly 200 nm in z centered about the point is sufficient. The range of d_0 at each iteration is limited to $(d - \Delta d_{max} < d_0 < d + \Delta d_{max})$.
6. Under Condition 2, the rearwards search is invoked. The first local minimum in MSE encountered during the search procedure is the solution.

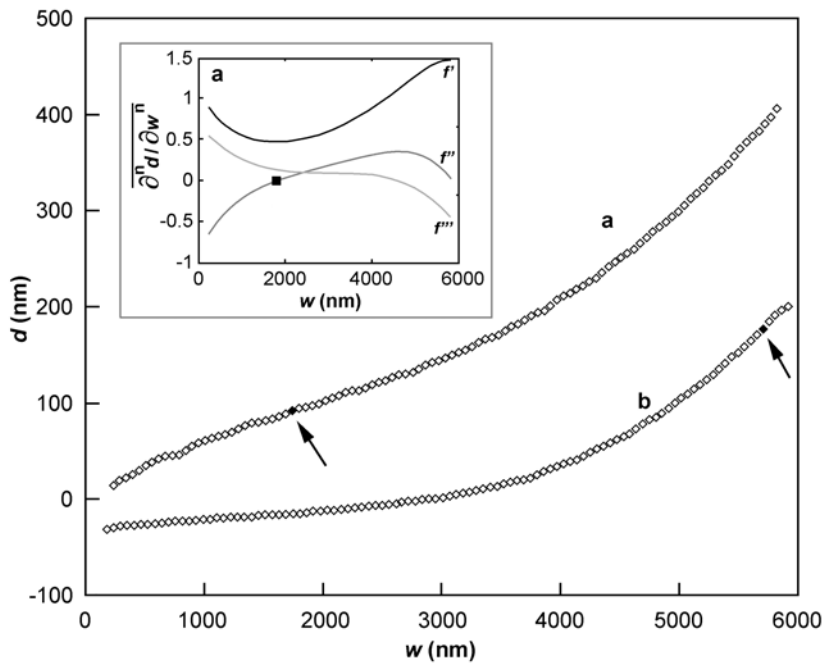


Figure 8. Two sample AFM datasets in which truncation was necessary to remove portions of the data that exhibited pronounced nonlinear behavior. Truncation points are indicated by the filled-in diamond symbols. In curve “a”, tip-sample repulsion is the likely cause of the absence of an obvious non-contact region; the effect is less pronounced in curve “b”. Determination of the truncation point is shown in the inset ($\partial^2 d / \partial w^2 = 0$ and $\partial^2 d / \partial w^2 > 0$); points to the left of the inflection are discarded. In curve “b”, the inflection point towards the end of the curve is identified in a like manner; points subsequent to the beginning of this downturn are discarded.

Discussion

Limitations of the method

There are a number of important issues to consider when applying the analysis methods presented in the prior sections. Foremost is that the mathematical representations, including the adhesive contact models, are based on linear elasticity theory. Intrinsic to the theory are the requirements of material isotropy and homogeneity, infinitesimal deformation (i.e., the sample can be approximated by an infinite half-space), and geometric linearity (i.e., deformations that do not exceed the linear stress-strain regime). Isotropy and homogeneity are length scale-dependent properties that can be defined by the size of the indenter; many materials that are isotropic and homogeneous at the macroscopic scale exhibit anisotropy and inhomogeneity to varying degrees at shorter length scales. The size of the indenter can be chosen such that it exceeds the scale at which anisotropy and inhomogeneity begin to emerge. In

probing biological tissues, for example, tips that are significantly smaller than the size of typical cells (on the order of tens of micrometers) can be used to delineate the cells from the surrounding matrix while larger probes can be used to measure the properties at the tissue level. In many experiments, the sample size in relation to the indentation depth and tip size is sufficiently large that the sample can be considered an infinite half-space. However, significant errors are incurred when the sample is so thin that the infinitesimal indentation assumption is violated. In such cases, allowances must be made for the effects of finite thickness [60, 75-77]. Dimitriadis *et al* [60] developed a correction to the Hertz equation that can be directly applied to experimental data and eliminates the complex numerical analysis required by other formulations.

Linearity of the stress-strain response is perhaps the most essential requirement in obtaining accurate, absolute measures of elastic properties using these methods. Boundary condition associated nonlinearities such as slip and temporary loss of contact between surfaces are generally of no concern in the indentation of a soft material by a rigid probe. However, the assumption of material and geometric linearity requires careful consideration of experimental conditions. For example, great care must be exercised in using sharp, tapered tips for probing the elasticity of soft materials because of the large strains induced even at small deformations [51, 52, 60]. Materials that exhibit nonlinearity and even plasticity at large deformations when indented with a spherical indenter have been shown to undergo an initial, linear elastic deformation [78, 79]. If the strain at which the transition from linear elastic to nonlinear behavior occurs is known, the maximum indentation depth can be limited to the linear regime. Two examples of material nonlinearity are shown in Figure 9. A transition from linear to nonlinear response is evident in the biological sample, where the fit using the complete dataset (maximum strain of ~30%) yields a poor fit as indicated by the relatively high MSE. By truncating the data to a maximum strain of ~20%, a drastic improvement in the fit is achieved, along with a large reduction in the predicted Young's modulus. In the synthetic polymer gel [34, 56], the two fits are equally good although some visually undetectable strain-hardening occurs at higher strains as indicated by the increase in magnitude of Young's modulus. This was found to be true at other polymer concentrations [34], as shown in Figure 10. In practice, if the linear strain threshold is unknown, it may be necessary to perform some indentations to various depths in order to establish a deflection cutoff. Excessive excursion beyond the linear limit is not advisable because it may result in plastic deformation. Truncation of a disproportionately large segment of data may also adversely affect accuracy by reducing the number of points included in the regression analysis.

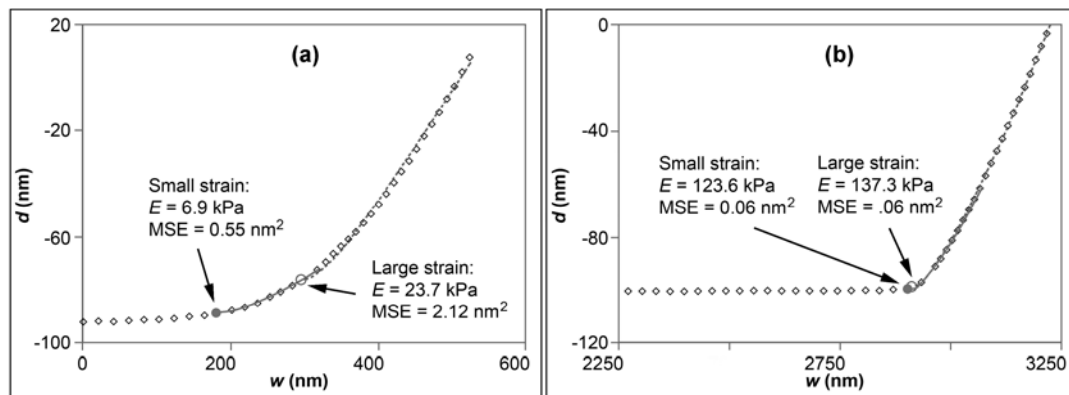


Figure 9. Two different examples of material nonlinearity in nanoindentation (AFM tip extension curves with every fifth to tenth point plotted). A polystyrene sphere with a diameter of $9.6 \mu\text{m}$ was used in both cases. Fits evaluated at a maximum normal strain of approximately 20% are represented by solid gray lines with contact points indicated by solid gray circles; fits evaluated up to maximum indentation are represented by dashed gray lines with contact points indicated by open circles. Also shown are the extracted values of Young's modulus and the MSE of the fits. Arrows point to the contact points. (a) The example on the left shows the indentation behavior of a biological specimen (cell-rich, $60 \mu\text{m}$ thick, longitudinally sectioned cartilage from the femoral head of a one-day old mouse; unpublished data). (b) The example on the right shows the behavior of a fully swollen, crosslinked poly(vinyl alcohol) gel previously described by the authors [34, 56].

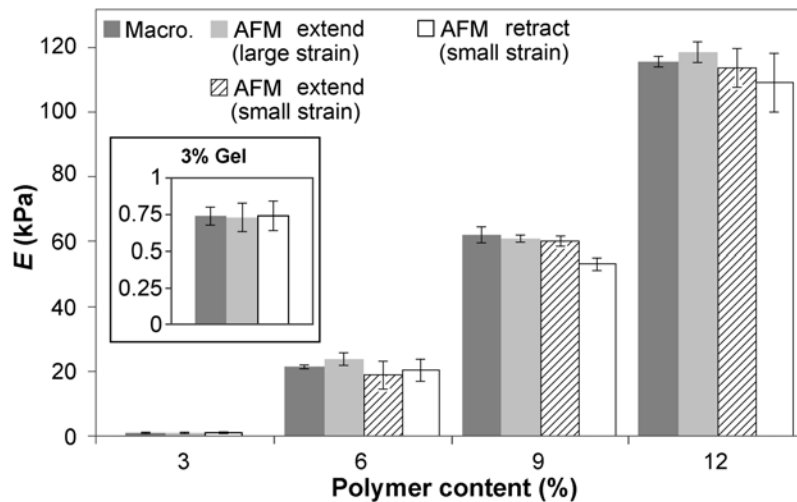


Figure 10. Results (mean \pm standard deviation) of macroscopic compression and AFM nanoindentation performed on poly(vinyl alcohol) gels of constant crosslink density and different initial polymer concentrations. The “force-volume” raster method was used to perform at least 256 separate indentations on each sample. AFM extension curves were evaluated at high strain (maximum indentation depth) and at small strain (data truncated at 20–25% strain). Retraction curves were evaluated at small strain only. Data from Lin *et al* [34, 56].

Large-strain constitutive laws such as the Mooney-Rivlin model and its specialized forms (e.g., the neo-Hookean equation) can be used to describe the deformation of many soft materials including those that exhibit rubber-like behavior [80, 81]. Arruda and Boyce [82] formulated a network model with only two material constants (initial shear modulus and extensibility of the eight chains in the network) that was shown by Liu and coworkers [83] to be applicable to biological tissues. However, use of these models has been largely limited to finite element and other numerical methods. The unavailability of large-strain contact mechanics models that can be easily applied to experimental data currently restricts the large-scale utility of nanoindentation to the testing of materials that are at least governed by linear constitutive laws during an initial deformation phase.

Effects of tip-sample interactions

The most prevalent form of tip-sample interaction is adhesion as the tip is pulled away from the sample; these interactions served as the motivation in the development of the JKR, DMT, and MD theories. The theories have been applied successfully by a number of researchers to the adhesion-influenced nanoindentation of synthetic polymers [26, 56, 59, 69]. Figure 11 shows typical results from the fitting of AFM retraction curves obtained from tests we conducted on poly(vinyl alcohol) gels. The comprehensive algorithm outlined previously was used to process all data summarized in Figure 10 – Hertzian analysis was utilized in all extension curves due to the absence of significant adhesion while adhesive analysis was invoked in the retraction curves for the 6% and 12% gels. Differences between extension and retraction results are attributed to slight hysteresis in the loading-unloading cycle [84]. When adhesive interactions are large enough to warrant use of the modified theories, application of Hertzian models should be avoided because of the potentially large errors. We verified the extent of these errors by using the Hertz equation to analyze the retraction curves of the force-volume dataset for the 12% gel from Figure 10 – the average Young's modulus decreased by greater than 20% and the average MSE increased nearly fivefold. Representative results from the analysis of a curve from the dataset are shown in Figure 12.

Tip-sample repulsion due to electrostatic forces represents another possible deviation from Hertzian behavior [85]. The effects on the indentation mechanics of like surface charges on the indenter and the sample have not been explored. While the electrostatic repulsive force as a function of the separation distance can be modeled mathematically [85], a complete model of the force-indentation behavior is lacking. It is obvious that the non-contact repulsive force is inversely proportional to the separation distance, reaching a maximum value of F_{es} at the point of contact; upon contact, the

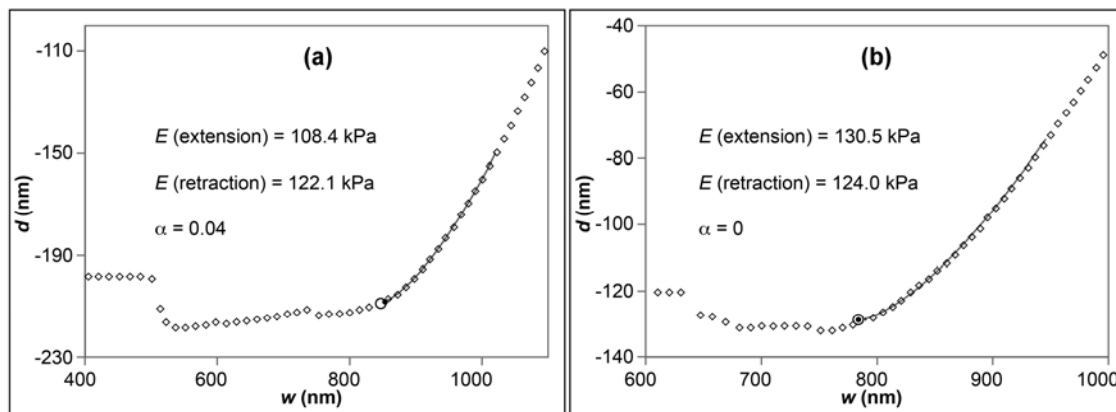


Figure 11. Two representative AFM retraction curves (every fifth to eighth point is plotted) from the indentation of a 12% poly(vinyl alcohol) gel [34, 56] showing large adhesive interactions between the 9.6 μm diameter polystyrene sphere and the sample. For the fitting, all datasets were restricted to $\sim 20\%$ strain. Fitted curves are represented by the solid lines. Also shown are the contact points (large open circles), points of zero indentation (small solid circles), and extracted values of Young's modulus and the PT parameter α . Young's modulus from the respective extension curves are shown for comparison. Note that the values of α are near the DMT limit of 0.

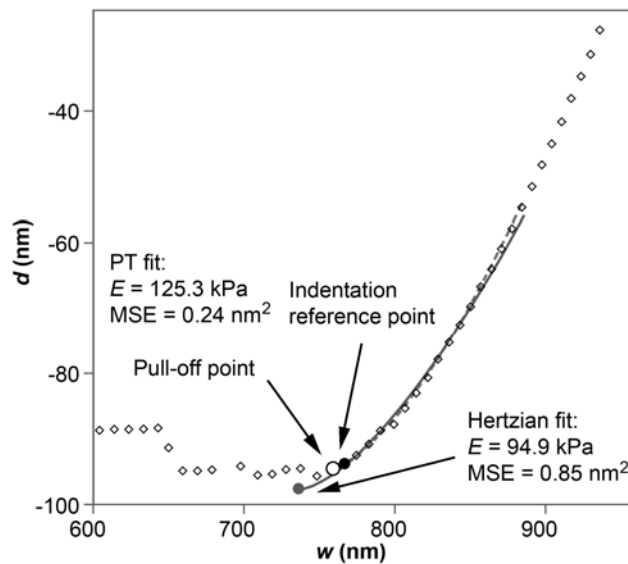


Figure 12. Representative example demonstrating the large errors that can be incurred when Hertzian models are applied to the analysis of datasets that exhibit significant adhesive interactions. For clarity, every fifth point is plotted. The sample, a poly(vinyl alcohol) gel with an initial polymer concentration of 12%, was indented with a 9.6 μm diameter polystyrene sphere. Note the poor fit of the Hertz equation (solid line) compared to the PT equation (dashed line) and the error of 25% in the extracted modulus value. In the majority of cases examined, the Hertzian models underestimate Young's moduli by similar margins.

force continues to increase as indentation proceeds. The consequence of this interaction is that the non-contact region may be indiscernible from the contact region, as typified by the curves in Figure 8 and Figure 13. If the surface-charge densities of the probe and sample are known, F_{es} can be estimated and used to locate the contact point. However, such properties are unknown in most experiments. In lieu of a theoretical basis for repulsion-influenced contact, use of the Hertzian models assumes that the electrostatic repulsive force at contact remains constant throughout the indentation cycle. Accordingly, the force-displacement or deflection-position curve in the contact region is simply offset by a distance corresponding to F_{es} , which has no effect on the elastic response of the sample. This is illustrated by example in Figure 13.

Experimental datasets in which the non-contact region is again indistinguishable and the Hertzian models fail to produce acceptable fits suggest the existence of more complex tip-sample interactions. The rearwards search method assumes that the effect of the interactive forces becomes negligible at large applied loads. By retaining only the portion of the dataset that obeys Hertzian contact, a surrogate contact point located off the data curve can be found. In Figure 14, the two uses of the rearwards search method (the handling of datasets with complex tip-sample interactions or datasets in which the contact point is not captured within the ramp) are demonstrated.

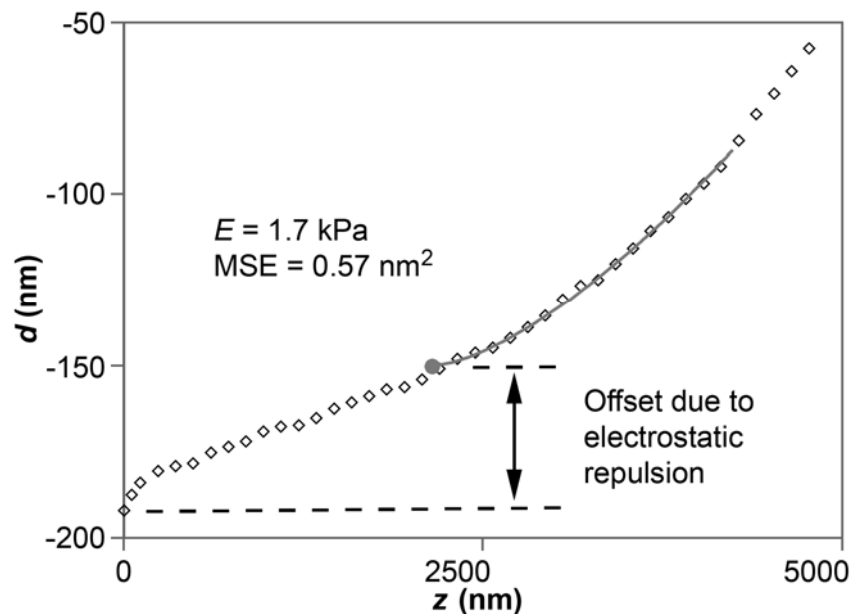


Figure 13. Example of repulsive tip-sample interactions that can be assumed to have negligible effect on the indentation mechanics. The sample is a 19-day old cartilage specimen grown from chicken sternum chondrocytes [35]. The probe tip was a 9.6 μm diameter polystyrene sphere. Every tenth point is plotted.

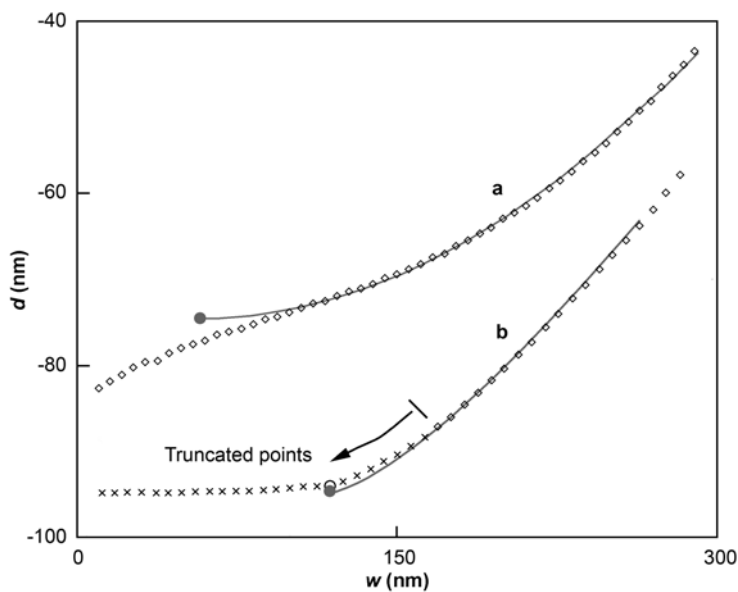


Figure 14. Examples illustrating the use of the rearwards search method. Curve “a” is the same curve as shown in Figure 8, but scaled for display purposes. Due to complex tip-sample interactions, a large portion of the curve was excluded from the analysis. In order to fit the remaining data with a Hertzian model, a surrogate contact point situated far from the actual data curve and found by the rearwards search is required. In curve “b”, a dataset that originally obeyed Hertzian mechanics was purposely truncated to eliminate the contact point (indicated by the open circle). The surrogate contact point identified by the rearwards search (filled circle) is accurate to within the level of noise in the data, with an error in the predicted Young’s modulus of 2%. Errors can be expected to increase with noise and the number of points truncated.

Other considerations

Control of experimental conditions and use of proper technique are essential for obtaining accurate and reproducible results, particularly with the AFM. These considerations include: sample preparation and tip selection to minimize interactions; calibration of voltage-deflection sensitivity; calibration of cantilever stiffness k_c (it is common to use the nominal value provided by the manufacturer, but uncertainties can be quite large and since E is directly proportional to k_c , potentially large errors in the extracted moduli can result); and setting of ramp size and ramp starting position. Also important are the geometry and dimensions of the indenter. Although the effects of tip shape and radius on AFM images are now well understood, their effects on elasticity measurements have not received the same level of attention. The practice of applying the Hertz model [86, 87] for indentation with blunt pyramidal tips is generally erroneous in the probing of soft materials because most commercial pyramidal tips have nominal tip radii on the order of 10-20 nm whereas maximum indentation depths of up to several hundred nanometers are typical in such samples. Similarly, use of the sharp conical or pyramidal models

[67, 88-92] is ill-advised in many situations because it introduces significant errors even when tip radii are small [34]. Other complications in the use of tapered tips to measure elastic properties are the large strains that can be induced and potential damage or alteration to the tip geometry subsequent to indenting a hard surface [93], required for instance, to calibrate the AFM voltage-deflection sensitivity. Whenever it is practicable, the use of spherical indenters is recommended for maximizing accuracy and consistency in the nanoindentation of soft materials [34, 60].

Final remarks

Advances in instrumented nanoindentation have made the technique viable for measuring the mechanical properties of soft materials at microscopic and submicron length scales. We reviewed here a number of the analysis techniques available for extracting elastic properties from AFM and DSN datasets, including a comprehensive scheme for the automated processing of large collections of data. The high-resolution force-mapping capabilities of the AFM and hybrid depth-sensing instruments have been exploited by investigators to map the elastic properties of systems as diverse as living cells and polymer blends. With the use of nanoindentation expanding to the characterization of an ever-wider range of biological and synthetic materials, the limitations of the linear elastic models become increasingly pronounced. Clearly, easy-to-implement and advanced mathematical models that account for complex surface interactions and other nonlinearities are needed. As these developments are realized, the importance and utility of nanoindentation will grow concomitantly.

Acknowledgment

This work was supported by the Intramural Research Program of the National Institutes of Health/National Institute of Child Health and Human Development.

Appendix

Processing of AFM data using the PT equation

1. Successively narrower segments of the non-contact region of the data to the point of maximum *negative* cantilever deflection are fit with a force law based on the Lennard-Jones potential. The form of this law is given by

$$d(r) = A \left[\left(\frac{B}{r} \right)^{12} - \left(\frac{B}{r} \right)^6 \right] + d_{ref} \quad (38)$$

$$r = 1 + C \frac{z^{(\kappa)} - z}{z^{(\kappa)}} \quad (39)$$

where r is a transformed variable representing the separation distance between the tip and sample, $(z^{(\kappa)}, d^{(\kappa)})$ is the point of maximum separation in the segment, C is a scale factor that controls the rate at which d drops to its minimum value, d_{ref} is a shift equal to the maximum value of d in the non-contact region, B is a constant equal to $(1/2)^{1/6}$, and $A = -4(d^{(\kappa)} - d_{ref})$. Points at greater separation than $(z^{(\kappa)}, d^{(\kappa)})$ are fit with the horizontal line $d = d^{(\kappa)}$, and the mean-square-error (MSE) of the two fits is computed. The $(z^{(\kappa)}, d^{(\kappa)})$ pair corresponding to the lowest aggregate MSE determines the value of d at the zero-force reference. Within the contact region, the z or w -coordinate of the force reference point is found by comparing values of the d -coordinate with d_1 . Figure 15 shows a sample power law fit to an actual dataset.

2. In tip retraction, the possibility of multiple releases due to events such as the unfolding of macromolecules adsorbed to the tip and sample surfaces, precludes designation of the point of maximum adhesive force as the point of separation (z', d') . The PT equation is applicable from the initial release point, as illustrated in the two sample datasets shown in Figure 16. To correctly identify (z', d') , a linear search in the direction of increasing z or w is initiated. At each iteration i , points for which $z < z^{(i)}$ are fit with a line while the remaining points are fit with a power function of the form

$$d = d^{(i)} + b(z - z^{(i)})^{3/2} \quad (40)$$

where b is the fitting parameter. An aggregate mean-square-error (MSE) is also calculated, with the contribution from the nonlinear fit given greater weight to offset the typically low MSE values from the zero-force, non-contact region. In most cases, multiplying the MSE of the nonlinear fit by a factor of 2 is sufficient. However, if the non-contact region comprises a disproportionately large segment of the data, a larger factor (e.g., 10) is necessary to identify the best fit to the contact region. From both sets of aggregate MSE values, the $(z^{(i)}, d^{(i)})$ pair corresponding to the lowest overall MSE is denoted (z^*, d^*) . In the interval bounded by (z^*, d^*) and (z_1, d_1) , the point corresponding to the smallest value of d , or the largest adhesive force, is taken to be the pull-off point (z', d') . Equation (31) can now be used to calculate the adhesive force F_{ad} .

3. To find the location of the indentation reference point (z_0, d_0) , first set Equation (22) to zero and perform algebraic manipulation to obtain

$$\left. \frac{F_n}{F_{ad}} \right|_{\delta=0} = (F_n / F_{ad})_0 = [(1+\alpha)S^{3/(4-2\beta)} - \alpha]^2 - 1 \quad (41)$$

- where S and β are defined by Equations (26) and (27) respectively. Next, iteratively increment the value of α from 0 to 1 using a sufficiently small step size (e.g., 0.01). Apply Equation (41) at each iteration to calculate $(F_n/F_{ad})_0$ and then use Equation (31) to determine d_0 .
4. In Equation (22), substitute Equation (30) for δ and Equation (31) for F_n . Reverse the roles of z and d as the independent and measured quantities, respectively, by rearranging the result to yield

$$z = z_0 + d - d_0 + \frac{a_0^2}{R} \left\{ \left[\frac{\alpha + \sqrt{1 + k_c(d - d_0)/F_{ad}}}{1 + \alpha} \right]^{4/3} - S \left[\frac{\alpha + \sqrt{1 + k_c(d - d_0)/F_{ad}}}{1 + \alpha} \right]^{2\beta} \right\} \quad (42)$$

- Regression analysis can now be performed to determine values of the parameters z_0 and a_0 in Equation (42).
5. Once the optimal location of (z_0, d_0) is found, Equation (24) is used to calculate the quantity \bar{a}_0 and the fitting parameter a_0^2/R yields the value of a_0 . To determine the interfacial energy, Equation (25) is used to find \bar{F}_{ad} , which is then substituted with F_{ad} into Equation (18) to calculate γ . The elastic constant of the indented material, E^* , is then obtained from Equation (17). With E^* known, Young's modulus is calculated using Equation (2).

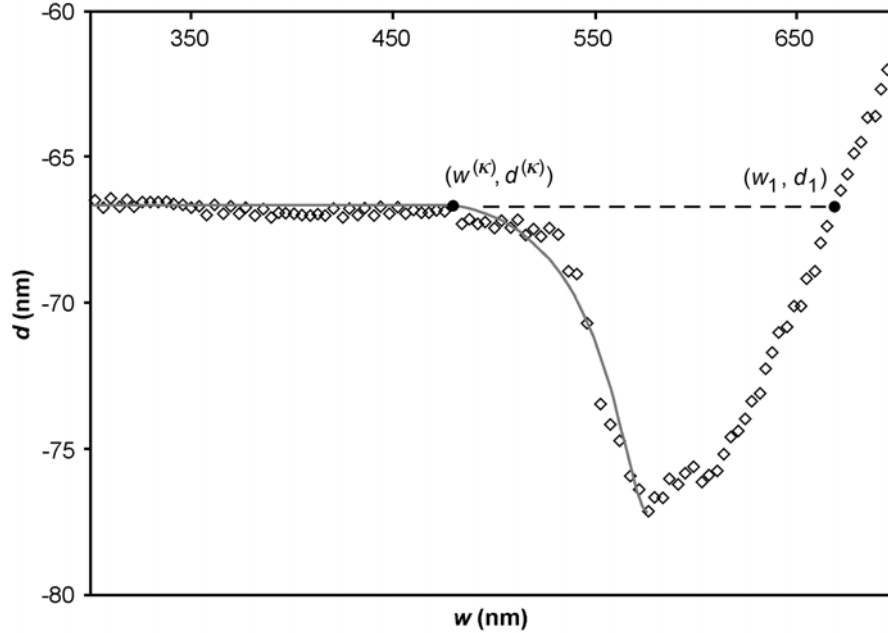


Figure 15. Portion of a sample dataset (every other point is shown) with a force law based on the Lennard-Jones potential fit to the non-contact portion of the data. The best fit is used to determine the zero-force reference point (w_1, d_1) or (z_1, d_1) .

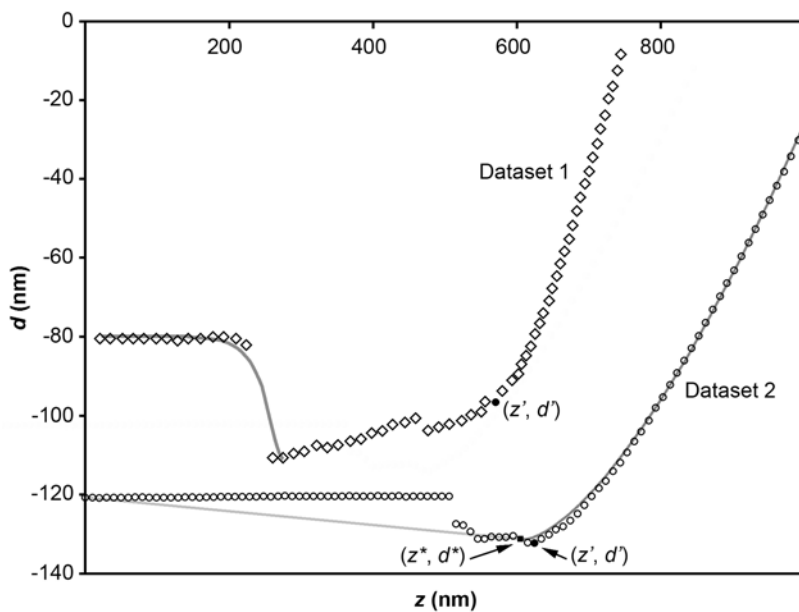


Figure 16. Two sample retraction datasets in which multiple release points are evident (every fifth to eight point is plotted). In both, the initial release point (z' , d') is indicated. The power-law fit based on the Lennard-Jones potential is shown for Dataset 1 by the gray curve. For Dataset 2, the combined fit using linear and 3/2 power functions is shown, with (z^*, d^*) being the point for which the aggregate mean-square-error is minimized. (z^*, d^*) is the point for which d is minimized in the interval bracketed by (z^*, d^*) and the force reference point.

References

1. Tabor, D., *The Hardness of Metals*. 1951, Oxford: Oxford University Press.
2. Syed Asif, S.A., R.J. Colton, and K.J. Wahl, *Nanoscale surface mechanical property measurements: force modulation techniques applied to nanoindentation*, in *Interfacial Properties on the Submicrometer Scale*, J. Frommer and R.M. Overney, Editors. 2001, ACS/Oxford University Press: Washington, DC. p. 198-215.
3. VanLandingham, M.R., *Review of instrumented indentation*. J Res Natl Inst Stand Technol, 2003. 108: p. 249-65.
4. Pethica, J.B., R. Hutchings, and W.C. Oliver, *Hardness measurement at penetration depths as small as 20 nm*. Philosophical Mag A, 1983. 48: p. 593-606.
5. Binnig, G., C.F. Quate, and C. Gerber, *Atomic force microscope*. Phys Rev Lett, 1986. 56: p. 930-3.
6. Joyce, S.A. and J.E. Houston, *A new force sensor incorporating force-feedback control for interfacial force microscopy*. Rev Sci Instrum, 1991. 62: p. 710-5.
7. Syed Asif, S.A., K.J. Wahl, R.J. Colton, and O.L. Warren, *Quantitative imaging of nanoscale mechanical properties using hybrid nanoindentation and force modulation*. J Appl Phys, 2001. 90: p. 1192-200.
8. Warren, O.L., J.F. Graham, and P.R. Norton, *Tapping mode imaging with an interfacial force microscope*. Rev Sci Instrum, 1997. 68: p. 4124-31.

9. Jandt, K.D., *Atomic force microscopy of biomaterials surfaces and interfaces*. Surf Sci, 2001. 491: p. 303-32.
10. Radmacher, M., *Measuring the elastic properties of biological samples with the AFM*. IEEE Eng Med Biol Mag, 1997. 16: p. 47-57.
11. Hoque, E., J.A. Derose, P. Hoffmann, H.J. Mathieu, B. Bhushan, and M. Cichomski, *Phosphonate self-assembled monolayers on aluminum surfaces*. J Chem Phys, 2006. 124: p. 174710.
12. Qian, L., X. Xiao, Q. Sun, and T. Yu, *Anomalous relationship between hardness and wear properties of a superelastic nickel-titanium alloy*. Appl Phys Lett, 2004. 84: p. 1076-8.
13. Tocha, E., H. Schonherr, and G.J. Vancso, *Quantitative nanotribology by AFM: a novel universal calibration platform*. Langmuir, 2006. 22: p. 2340-50.
14. Habelitz, S., S.J. Marshall, G.W. Marshall, and M. Balooch, *The functional width of the dentino-enamel junction determined by AFM-based nanoscratching*. J Struct Biol, 2001. 135: p. 294-301.
15. Mendez-Vilas, A., J. Diaz, M.G. Donoso, A.M. Gallardo-Moreno, and M.L. Gonzalez-Martin, *Ultrastructural and physico-chemical heterogeneities of yeast surfaces revealed by mapping lateral-friction and normal-adhesion forces using an atomic force microscope*. Antonie Van Leeuwenhoek, 2006. 89: p. 495-509.
16. Stiernstedt, J., N. Nordgren, L. Wagberg, H. Brumer III, D.G. Gray, and M.W. Rutland, *Friction and forces between cellulose model surfaces: A comparison*. J Colloid Interface Sci, 2006. 303: p. 117-23.
17. Cho, J.H., D.H. Lee, H.S. Shin, S.K. Pattanayek, C.Y. Ryu, and K. Cho, *Exploiting poly(dimethylsiloxane)-modified tips to evaluate frictional behavior by friction force microscopy*. Langmuir, 2004. 20: p. 11499-503.
18. El Kirat, K., I. Burton, V. Dupres, and Y.F. Dufrene, *Sample preparation procedures for biological atomic force microscopy*. J Microsc, 2005. 218: p. 199-207.
19. Fotiadis, D., S. Scheuring, S.A. Muller, A. Engel, and D.J. Muller, *Imaging and manipulation of biological structures with the AFM*. Micron, 2002. 33: p. 385-97.
20. Kienberger, F., A. Ebner, H.J. Gruber, and P. Hinterdorfer, *Molecular recognition imaging and force spectroscopy of single biomolecules*. Acc Chem Res, 2006. 39: p. 29-36.
21. Silva, L.P., *Imaging proteins with atomic force microscopy: an overview*. Curr Protein Peptide Sci, 2005. 6: p. 387-95.
22. Kawakami, M., K. Byrne, D.J. Brockwell, S.E. Radford, and D.A. Smith, *Viscoelastic study of the mechanical unfolding of a protein by AFM*. Biophys J, 2006. 91: p. L16-8.
23. Cheng, L., X. Xia, W. Yu, L.E. Scriven, and W.W. Gerberich, *Flat-punch indentation of viscoelastic material*. J Polymer Sci B, 2000. 38: p. 10-22.
24. Yang, G., N. Rao, Z. Yin, and D.M. Zhu, *Probing the viscoelastic response of glassy polymer films using atomic force microscopy*. J Colloid Interface Sci, 2006. 297: p. 104-11.
25. Wahl, K.J., S.A. Asif, J.A. Greenwood, and K.L. Johnson, *Oscillating adhesive contacts between micron-scale tips and compliant polymers*. J Colloid Interface Sci, 2006. 296: p. 178-88.

26. Sun, Y. and G.C. Walker, *Viscoelastic response of poly(dimethylsiloxane) in the adhesive interaction with AFM tips*. Langmuir, 2005. 21: p. 8694-702.
27. Feng, G. and A.H.W. Ngan, *Effects of creep and thermal drift on modulus measurement using depth-sensing indentation*. J Mater Res, 2002. 17: p. 660-8.
28. Ngan, A.H.W., H.T. Wang, B. Tang, and K.Y. Sze, *Correcting power-law viscoelastic effects in elastic modulus measurement using depth-sensing indentation*. Int J Solids Struct, 2005. 42: p. 1831-46.
29. Darling, E.M., S. Zauscher, and G. Guilak, *Viscoelastic properties of zonal articular chondrocytes measured by atomic force microscopy*. Osteoarthritis Cartilage, 2006. 14: p. 571-9.
30. Fan, Z. and J.Y. Rho, *Effects of viscoelasticity and time-dependent plasticity on nanoindentation measurements of human cortical bone*. J Biomed Mater Res A, 2003. 67: p. 208-14.
31. Mathur, A.B., A.M. Collinsworth, W.M. Reichert, W.E. Kraus, and G.A. Truskey, *Endothelial, cardiac muscle and skeletal muscle exhibit different viscous and elastic properties as determined by atomic force microscopy*. J Biomech, 2001. 34: p. 1545-53.
32. Radmacher, M., M. Fritz, C.M. Kacher, J.P. Cleveland, and P.K. Hansma, *Measuring the viscoelastic properties of human platelets with the atomic force microscope*. Biophys J, 1996. 70: p. 556-67.
33. Rico, F., P. Roca-Cusachs, N. Gavara, R. Farre, M. Rotger, and D. Navajas, *Probing mechanical properties of living cells by atomic force microscopy with blunted pyramidal cantilever tips*. Phys Rev E Stat Nonlin Soft Matter Phys, 2005. 72: p. 021914.
34. Lin, D.C., E.K. Dimitriadis, and F. Horkay, *Robust strategies for automated AFM force curve analysis: I. Non-adhesive indentation of soft, inhomogeneous materials*. J Biomech Eng, 2007. In press.
35. Horkay, F., I. Horkayne-Szakaly, and P.J. Basser, *Measurement of the osmotic properties of thin polymer films and biological tissue samples*. Biomacromolecules, 2005. 6: p. 988-93.
36. Hertz, H., *Über die berührung fester elastischer korper (on the contact of elastic solids)*. J Reini Angew Math, 1881. 5: p. 12-23.
37. Boussinesq, J., *Applications des Potentiels a l'Etude de l'Equilibre et du Mouvement des Solides Elastiques*. 1885, Paris: Gauthier-Villars.
38. Love, A.E.H., *Boussinesq's problem for a rigid cone*. Quart J Math, 1939. 10: p. 161-75.
39. Segedin, C.M., *The relation between load and penetration for a spherical punch*. Mathematika, 1957. 4: p. 156-61.
40. Landau, L.D. and E.M. Lifshitz, *Theory of Elasticity*. 1959, Oxford: Pergamon Press.
41. Sneddon, I.N., *The relation between load and penetration in the axisymmetric Boussinesq problem for a punch of arbitrary profile*. Int J Eng Sci, 1965. 3: p. 47-57.
42. Johnson, K.L., K. Kendall, and A.D. Roberts, *Surface energy and the contact of elastic solids*. Proc R Soc Lond A, 1971. 324: p. 301-13.
43. Derjaguin, B.V., V.M. Muller, and Y.P. Toporov, *Effect of contact deformations on the adhesion of particles*. J Colloid Interface Sci, 1975. 53: p. 314-26.

44. Johnson, K.L. and J.A. Greenwood, *An adhesion map for the contact of elastic spheres*. J Colloid Interface Sci, 1997. 192: p. 326-333.
45. Tabor, D., *Surface forces and surface interactions*. J Colloid Interface Sci, 1976. 58: p. 2-13.
46. Muller, V.M., V.S. Yushchenko, and B.V. Derjaguin, *On the influence of molecular forces on the deformation of an elastic sphere and its sticking to a rigid plane*. J Colloid Interface Sci, 1980. 77: p. 91-101.
47. Greenwood, J.A., *Adhesion of elastic spheres*. Proc R Soc Lond A, 1997. 453: p. 1277-97.
48. Maugis, D., *Adhesion of spheres: The JKR-DMT transition using a Dugdale model*. J Colloid Interface Sci, 1992. 150: p. 243-69.
49. Johnson, K.L., *Contact Mechanics*. 1985, Cambridge: Cambridge University Press.
50. Barber, J.R., *Elasticity*. 2nd ed. Solid Mechanics and its Applications, ed. G.M.L. Gladwell. Vol. 107. 2002, Dordrecht: Kluwer Academic.
51. Costa, K.D. and F.C.P. Yin, *Analysis of indentation: implications for measuring mechanical properties with atomic force microscopy*. J Biomech Eng, 1999. 121: p. 462-71.
52. Bilodeau, G., *Regular pyramid punch problem*. J Appl Mech, 1992. 59: p. 519-23.
53. Na, S., Z. Sun, G.A. Meiningen, and J.D. Humphrey, *On atomic force microscopy and the constitutive behavior of living cells*. Biomech Model Mechanobiol, 2004. 3: p. 75-84.
54. Burnham, N.A., R.J. Colton, and H.M. Pollock, *Interpretation issues in force microscopy*. J Vac Sci Technol, 1991. 9: p. 2548-56.
55. Pietrement, O. and M. Troyon, *General equations describing elastic indentation depth and normal contact stiffness versus load*. J Colloid Interface Sci, 2000. 226: p. 166-71.
56. Lin, D.C., E.K. Dimitriadis, and F. Horkay, *Robust strategies for automated AFM force curve analysis: II. Adhesion-Influenced indentation of soft, elastic materials*. J Biomech Eng, 2007. Submittted.
57. Carpick, R.W., D.F. Ogletree, and M. Salmeron, *A general equation for fitting contact area and friction vs load measurements*. J Colloid Interface Sci, 1999. 211: p. 395-400.
58. Maugis, D., *Extension of the Johnson-Kendall-Roberts theory of the elastic contact of spheres to large contact radii*. Langmuir, 1995. 11: p. 679-82.
59. Sun, Y., B. Akhremitchev, and G.C. Walker, *Using the adhesive interaction between atomic force microscopy tips and polymer surfaces to measure the elastic modulus of compliant samples*. Langmuir, 2004. 20: p. 5837-45.
60. Dimitriadis, E.K., F. Horkay, J. Maresca, B. Kachar, and R.S. Chadwick, *Determination of elastic moduli of thin layers of soft material using the atomic force microscope*. Biophys J, 2002. 82: p. 2798-810.
61. A-Hassan, E., W.F. Heinz, M.D. Antonik, N.P. D'Costa, S. Nageswaran, C. Schoenenberger, and J.H. Hoh, *Relative microelastic mapping of living cells by atomic force microscopy*. Biophys J, 1998. 74: p. 1564-78.
62. Oliver, W.C. and G.M. Pharr, *An improved technique for determining hardness and elastic modulus using load and displacement sensing indentation experiments*. J Mater Res, 1992. 7: p. 1564-83.

63. Geissler, E. and A.M. Hecht, *The Poisson ratio in polymer gels*. Macromolecules, 1980. 13: p. 1276-80.
64. Mow, V.C., W.M. Lai, and M.H. Holmes, *Advanced theoretical and experimental techniques in cartilage research*, in *Biomechanics: Principles and Applications*, R. Huiskes, D. Van Campen, and J. Dewijn, Editors. 1982, Martinus Nijhoff: The Hague.
65. Nyland, L.R. and D.W. Maughan, *Morphology and transverse stiffness of Drosophila myofibrils measured by atomic force microscopy*. Biophys J, 2000. 78: p. 1490-7.
66. Jaasma, M.J., W.M. Jackson, and T.M. Keaveny, *Measurement and characterization of whole-cell mechanical behavior*. Ann Biomed Eng, 2006. 34: p. 748-58.
67. Radmacher, M., *Measuring the elastic properties of living cells by the atomic force microscope*. Methods Cell Biol, 2002. 68: p. 67-90.
68. Kolambkar, Y.M., *Extracting mechanical properties of cells/biomaterials using the atomic force microscope*. Master's thesis, 2004. University of Cincinnati, Cincinnati, OH, <http://www.ohiolink.edu>.
69. Cao, Y., D. Yang, and W. Soboyejoy, *Nanoindentation method for determining the initial contact and adhesion characteristics of soft polydimethylsiloxane*. J Mater Res, 2005. 20: p. 2004-11.
70. Hofmann, U.G., C. Rotsch, W.J. Parak, and M. Radmacher, *Investigating the cytoskeleton of chicken cardiocytes with the atomic force microscope*. J Struct Biol, 1997. 119: p. 84-91.
71. Rotsch, C., F. Braet, E. Wisse, and M. Radmacher, *AFM imaging and elasticity measurements on living rat liver macrophages*. Cell Biol Int, 1997. 21: p. 685-96.
72. Jaasma, M.J., W.M. Jackson, and T.M. Keaveny, *The effects of morphology, confluence, and phenotype on whole-cell mechanical behavior*. Ann Biomed Eng, 2006. 34: p. 759-68.
73. Haga, H., S. Sasaki, K. Kawabata, E. Ito, T. Ushiki, and T. Sambongi, *Elasticity mapping of living fibroblasts by AFM and immunofluorescence observation of the cytoskeleton*. Ultramicroscopy, 2000. 82: p. 253-8.
74. Nitta, T., H. Haga, K. Kawabata, K. Abe, and T. Sambongi, *Comparing microscopic with macroscopic elastic properties of polymer gel*. Ultramicroscopy, 2000. 82: p. 223-6.
75. Hayes, W.C., L.M. Keer, G. Herrmann, and L.F. Mockros, *A mathematical analysis for indentation tests of articular cartilage*. J Biomech, 1972. 5: p. 541-51.
76. Jaffar, M.J., *A numerical solution for axisymmetric contact problems involving rigid indenters on elastic layers*. J Mech Phys Solids, 1988. 36: p. 401-16.
77. Matthewson, M.J., *Axi-symmetric contact on thin compliant coatings*. J Mech Phys Solids, 1981. 29: p. 89-113.
78. Francis, H.A., *Phenomenological analysis of plastic spherical indentation*. J Eng Mater Technol, 1976. 98: p. 272-81.
79. Ingman, D., J. Suzdalnitsky, and M. Zeifman, *Constitutive dynamic-order model for nonlinear contact phenomena*. J Appl Mech, 2000. 67: p. 383-90.
80. Aklonis, J.J. and W.J. MacKnight, *Introduction to Polymer Viscoelasticity*. 1983, New York: John Wiley and Sons.

81. Treloar, L.R.G., *The Physics of Rubber Elasticity*. 3rd ed. 1975, Oxford: Oxford University Press.
82. Arruda, E.M. and M.C. Boyce, *A three-dimensional constitutive model for the large stretch behavior of rubber elastic materials*. J Mech Phys Solids, 1993. 41: p. 389-412.
83. Liu, Y., A.E. Kerdok, and R.D. Howe, *A nonlinear finite element model of soft tissue indentation*, in *Medical Simulation: International Symposium - ISMS 2004*, S. Cotin and D.N. Metaxas, Editors. 2004, Springer-Verlag: Berlin.
84. Butt, H., B. Capella, and M. Kappl, *Force measurements with the atomic force microscope: Technique, interpretation and applications*. Surf Sci Reports, 2005. 59: p. 1-152.
85. Heinz, W.F. and J.H. Hoh, *Spatially resolved force spectroscopy of biological surfaces using the atomic force microscope*. Trends Biotechnol, 1999. 17: p. 143-50.
86. Nie, H.Y., M. Motomatsu, W. Mizutani, and H. Tokumoto, *Local elasticity measurement on polymers using atomic force microscopy*. Thin Solid Films, 1996. 273: p. 143-8.
87. Tomkoria, S., R.V. Patel, and J.J. Mao, *Heterogeneous nanomechanical properties of superficial and zonal regions of articular cartilage of the rabbit proximal radius condyle by atomic force microscopy*. Med Eng Phys, 2004. 26: p. 815-22.
88. Alcaraz, J., L. Buscemi, M. Grabulosa, X. Trepaut, B. Fabry, R. Farre, and D. Navajas, *Microrheology of human lung epithelial cells measured by atomic force microscopy*. Biophys J, 2003. 84: p. 2071-9.
89. Domke, J. and M. Radmacher, *Measuring the elastic properties of thin polymer films with the atomic force microscope*. Langmuir, 1998. 14: p. 3320-5.
90. Jiao, Y. and T.E. Schaffer, *Accurate height and volume measurements on soft samples with the atomic force microscope*. Langmuir, 2004. 20: p. 10038-45.
91. Rotsch, C., K. Jacobson, and M. Radmacher, *Dimensional and mechanical dynamics of active and stable edges in motile fibroblasts investigated by using atomic force microscopy*. Proc Natl Acad Sci U S A, 1999. 96: p. 921-6.
92. Tao, N.J., S.M. Lindsay, and S. Lees, *Measuring the microelastic properties of biological material*. Biophys J, 1992. 63: p. 1165-9.
93. Kopycinska-Muller, M., R.H. Geiss, and D.C. Hurley, *Contact mechanics and tip shape in AFM-based nanomechanical measurements*. Ultramicroscopy, 2006. 106: p. 466-74.